

# Quantal diffusion approach for multinucleon transfer processes in the $^{58,64}\text{Ni} + ^{208}\text{Pb}$ reactions: Toward the production of unknown neutron-rich nuclei

Kazuyuki Sekizawa<sup>1,2,\*</sup> and Sakir Ayik<sup>3,†</sup>

<sup>1</sup>Center for Transdisciplinary Research, Institute for Research Promotion, Niigata University, Niigata 950-2181, Japan

<sup>2</sup>Division of Nuclear Physics, Center for Computational Sciences, University of Tsukuba, Ibaraki 305-8577, Japan

<sup>3</sup>Physics Department, Tennessee Technological University, Cookeville, Tennessee 38505, USA

(Dated: July 29, 2020)

**Background:** In recent years, substantial efforts have been made for the study of multinucleon transfer reactions at energies around the Coulomb barrier both experimentally and theoretically, aiming at the production of unknown neutron-rich heavy nuclei. It is crucial to provide reliable theoretical predictions based on microscopic theories with sufficient predictive power.

**Purpose:** This paper aims to clarify the applicability of the quantal diffusion approach based on the stochastic mean-field (SMF) theory for multinucleon transfer processes. Isotope production cross sections are evaluated for the reactions of  $^{64}\text{Ni} + ^{208}\text{Pb}$  at  $E_{c.m.} = 268$  MeV and  $^{58}\text{Ni} + ^{208}\text{Pb}$  at  $E_{c.m.} = 270$  MeV and are compared with available experimental data.

**Methods:** Three-dimensional time-dependent Hartree-Fock (TDHF) calculations are carried out for a range of initial orbital angular momenta with Skyrme SLy4d functional. Quantal diffusion equations, derived based on the SMF theory, for variances and covariance of neutron and proton numbers of reaction products are solved, with microscopic drift and diffusion coefficients obtained from time evolution of occupied single-particle orbitals in TDHF. Secondary deexcitation processes, both particle evaporation and fission, are simulated by a statistical compound-nucleus deexcitation model, GEMINI++.

**Results:** Dynamics of a fast isospin equilibration process followed by a slow drift toward the mass symmetry are commonly observed, as expected. Various reaction outcomes are evaluated, including average mass and charge numbers of reaction products, total kinetic energy loss (TKEL), scattering angle, contact time, and production cross sections for primary and secondary products. By comparing with the experimental data, we find that SMF and TDHF quantitatively reproduce experimental data for few-nucleon-transfer channels around the average values. In contrast, for many-nucleon-transfer channels, we find that the SMF approach provides much better description of the experimentally measured isotopic distributions. The results underline the importance of beyond mean-field effects, especially one-body (mean-field) fluctuations and correlations, in describing multinucleon transfer processes. Moreover, through a combined analysis of SMF with a statistical model, GEMINI++, we find a significant contribution of transfer-induced fission, which is consistent with the experimental observation. In some cases, the SMF approach overestimates the isotopic width, requiring further improvements of the theoretical description. Possible ways to improve the description are discussed.

**Conclusions:** The SMF approach is designed to describe the quantum many-body problem according to an ensemble of mean-field trajectories, taking into account part of many-body correlations in the description. As it requires feasible computational costs comparable to the ordinary TDHF approach, together with further model improvements, it will be a promising tool in the search for optimal reaction conditions to produce yet-unknown neutron-rich heavy nuclei through the multinucleon transfer reaction.

## I. INTRODUCTION

This paper aims to develop a predictive microscopic approach for multinucleon transfer reactions to guide future experiments for production of yet-unknown neutron-rich heavy nuclei. The production of unknown neutron-rich isotopes is essential to develop our understanding of physics of atomic nuclei. Fragmentation, fission, and fusion processes have been successful to certainly extend the nuclear map of known isotopes [1]. However, there are regions where those methods have difficulty in producing unstable nuclei, typically located in the north-eastern part of the nuclear landscape, which is referred to as a ‘blank spot’ [2]. Study of such neutron-rich heavy isotopes is of paramount importance not only for nuclear structure, but also for nuclear astrophysics aspects. Experimental and theoretical investigations of nuclear shape and shell evolution in the region of neutron-rich nuclei [3] and the predicted island of stability in the superheavy region [4, 5] will

drive our understanding of the physics of atomic nuclei. In particular, properties of neutron-rich nuclei along the neutron magic number  $N = 126$  are crucial to uncover the detailed pathways of the  $r$ -process nucleosynthesis [6]. Those nuclei correspond to the last waiting point in the  $r$  process, providing the third peak structure at  $A \approx 195$  in the solar abundance. Besides, the region of superheavy nuclei has been explored by fusion reactions that could produce neutron deficient isotopes with respect to the  $\beta$ -stability line [4, 5]. The multinucleon transfer reactions might be a possible alternative to produce neutron-rich superheavy nuclei in the yet-unreached island of stability, although further investigations are mandatory [7]. For the history, current status, and future prospect of the experimental endeavor for new isotopes production with the multinucleon transfer reaction, we refer readers to a recent comprehensive review [7] and references therein.

For the study of multinucleon transfer reactions, semiclassical models such as GRAZING [8, 9] and complex Wentzel-Kramers-Brillouin (CWKB) [10] have been successfully used to describe transfer processes at peripheral collisions. GRAZING has been incorporated with a statistical model to take into account the effect of fission, such as GRAZING-F [11] or

\* sekizawa@phys.sc.niigata-u.ac.jp

† ayik@tntech.edu

GRAZING plus GEMINI++ [12]. Although it offers quantitative predictions for few-nucleon transfers, it substantially underestimates many-nucleon transfer processes due to missing contributions from deep-inelastic collisions at small impact parameters. The so-called dinuclear system (DNS) model, initially developed for fusion reactions, has been applied also for multinucleon transfer and quasifission processes in damped collisions. In the latter model, the probability distribution for production of various isotopes are derived either by solving a master equation for mass and/or charge asymmetry [13–16] or using a simplified statistical expression [17–21]. To include contributions from peripheral collisions, which are absent in the DNS model, a simple hybrid called DNS+GRAZING has been considered in the literature [22, 23]. A Langevin-type dynamical model has also been successful in describing multinucleon transfer, quasifission, and fusion, in a unified way [24, 25] and has been further improved in Refs. [26, 27]. On the other hand, there are microscopic models that treat explicitly nucleonic degrees of freedom such as improved quantum molecular dynamics (ImQMD) model [28–31]. Although the latter model still neglects the spin-orbit interaction, it has shown successes in describing mass, charge, and total kinetic energy (TKE) distributions. While the above-mentioned approaches have been extensively developed and successfully applied, they rely on phenomenology to a certain extent. In the present paper, we employ microscopic time-dependent self-consistent mean-field theories, such as time-dependent Hartree-Fock (TDHF) and its extension, which contains no adjustable parameters and with no artificial restrictions on the reaction dynamics. (See, the above mentioned references and review papers [7, 32–34], and references cited therein, for many other applications and discussions.)

The TDHF approach can properly describe the most probable dynamical path in low-energy heavy-ion reactions, resulting in a good description of total kinetic energy loss (TKEL) and scattering angle, as well as average neutron and proton numbers. This is supported by an extended variational principle of Balian and Vénéroni [35], which derives TDHF as a variation optimized for one-body observables [36]. With the help of the particle-number projection method [37], one can also extract the probability for production of each isotope. The particle-number projection method has been used to study multinucleon transfer processes in  $^{16}\text{O}+^{208}\text{Pb}$  [37],  $^{40,48}\text{Ca}+^{124}\text{Sn}$ ,  $^{40}\text{Ca}+^{208}\text{Pb}$ ,  $^{58}\text{Ni}+^{208}\text{Pb}$  [38, 39],  $^{24}\text{O}+^{16}\text{O}$  [40],  $^{18}\text{O}+^{206}\text{Pb}$  [41],  $^{64}\text{Ni}+^{238}\text{U}$  [39, 42],  $^{136}\text{Xe}+^{198}\text{Pt}$  [39],  $^{238}\text{U}+^{124}\text{Sn}$  [43],  $^{16}\text{O}+^{27}\text{Al}$  [44],  $^{58}\text{Ni}+^{124}\text{Sn}$  [45],  $^{132}\text{Sn}+^{208}\text{Pb}$  [46],  $^{136}\text{Xe}$ ,  $^{132}\text{Sn}+^{208}\text{Pb}$  [47], and  $^{136}\text{Xe}+^{194}\text{Ir}$  [48], at energies around the Coulomb barrier. It has been shown that TDHF works quite well in describing production cross sections quantitatively for transfer of a few nucleons around the average values. Recently, the TDHF approach has been combined with a statistical model to evaluate effects of secondary processes of excited reaction products [39, 45–50]. It has been quantified that TDHF underestimates production cross sections for many-nucleon transfer channels. This is related to the well-known drawback of the TDHF approach, that is, it cannot describe the fluctuations of the collective dynamics and severely underestimates the fragment mass and charge dispersions [51–55]. One should note that the particle-number

projection method does not go beyond TDHF, but it is just a technique to extract transfer probabilities from the TDHF wave function after collision [37, 38]. For a reliable, quantitative description of processes far apart from the mean trajectory, one must go beyond the standard TDHF description.

Recently, it has been shown that the description can be improved significantly by the use of time-dependent random phase approximation (TDRPA) which can be derived from the extended variational principle of Balian and Vénéroni [35]. The variation suitable for describing dispersions of one-body observables with a single Slater determinant gives rise to the TDRPA formula that takes into account one-body fluctuations and correlations around the TDHF average trajectory. TDRPA was applied to deep-inelastic collisions of  $^{16}\text{O}+^{16}\text{O}$  [53] and  $^{40}\text{Ca}+^{40}\text{Ca}$  [54], showing substantial improvements of the description. Recently, the TDRPA results of the width of fragment mass distribution for deep-inelastic  $^{60}\text{Ni}+^{60}\text{Ni}$  collisions were compared with the experimental data of  $^{58}\text{Ni}+^{60}\text{Ni}$  at the same center-of-mass energies, showing a remarkable quantitative agreement [55]. The results indicate that the one-body fluctuations incorporated by TDRPA are the predominant mechanism for the mass-width evolution in heavy-ion reactions at low energies. Furthermore,  $^{176}\text{Yb}+^{176}\text{Yb}$  collisions were investigated within the TDHF and TDRPA approaches and primary production cross sections were computed that suggest possible production of neutron-rich nuclei [56]. One should note, however, that, as was shown in Ref. [55], the TDRPA formula in the current form cannot be applied to asymmetric systems, which prevents systematic investigations for various projectile-target combinations within the TDRPA approach.

In the present paper, we investigate an alternative approach, called the stochastic mean-field (SMF) approach, proposed by Ayik in 2008 [57], which incorporates beyond mean-field fluctuations and correlations into the description. The original idea was to model the quantum many-body problem by an ensemble of time-dependent mean-field solutions by introducing initial mean-field fluctuations, akin to, in some sense, the derivation of quantum mechanics from Brownian particles [58]. Later, it was shown that the SMF treatment includes more than just the one-body fluctuations and correlations through a simplified Bogoliubov-Born-Green-Kirkwood-Yvon (BBGKY) hierarchy [59]. It can be shown that the SMF approach, while being applicable also to asymmetric systems, coincides analytically with the TDRPA formula in the small fluctuation limit [57, 60]. In recent years, there have been rapid developments and improvements in the description. In the initial stage of applications, a semiclassical treatment with the Wigner transformation and with the Markov approximation was employed [61–65]. In Ref. [66], a quantal expression of the diffusion coefficient was proposed, further refined by eliminating particle states from the expression with the completeness relation [67], which is expressed in terms of the single-particle orbitals from the mean-field theory. The quantal expression was applied for central collisions of symmetric systems,  $^{28}\text{O}+^{28}\text{O}$ ,  $^{40,48}\text{Ca}+^{40,48}\text{Ca}$ , and  $^{56}\text{Ni}+^{56}\text{Ni}$ , just below the Coulomb barrier, and also for head-on collisions of  $^{238}\text{U}+^{238}\text{U}$  [68]. Finally, the quantal diffusion description was generalized for non-central collisions [69].

The approach was successfully applied to  $^{48}\text{Ca}+^{238}\text{U}$  [69],  $^{58,60}\text{Ni}+^{60}\text{Ni}$  [70],  $^{136}\text{Xe}+^{208}\text{Pb}$  [71, 72], and  $^{48}\text{Ca}+^{208}\text{Pb}$  [73] systems. We mention here that the SMF approach has also been applied in other contexts such as spinodal instabilities of nuclear matter [74–80], symmetry breaking [81], Fermionic Hubbard clusters [82], as well as nuclear fission [83]. (For other mean-field approaches with stochastic extensions, see discussions in, e.g., Refs. [60, 84], and references therein.)

In this work, we analyze the multinucleon transfer processes in the  $^{64}\text{Ni}+^{208}\text{Pb}$  reaction at  $E_{\text{c.m.}} = 268$  MeV and the  $^{58}\text{Ni}+^{208}\text{Pb}$  reaction at  $E_{\text{c.m.}} = 270$  MeV, for which experimental data are available [85, 86]. Because of the relatively large isospin asymmetry of the systems, a fast isospin equilibration process takes place. Also, since the systems have a relatively large charge product,  $Z_{\text{P}}Z_{\text{T}} = 2296$ , an onset of quasifission emerges accompanying a transfer of many nucleons from heavy to light nuclei that drives the system toward the mass symmetry. The comparison of these two systems at almost the same center-of-mass energy will reveal detailed reaction mechanisms, especially isospin dependence of the dynamics. In the experiments by Królás *et al.* [85, 86], a thick target was utilized and a full set of reaction products were thoroughly analyzed, which were stopped in the target material. They performed elaborated analyses of in-beam and off-line  $\gamma$ - $\gamma$  coincidences [86], supplemented with off-line radioactivity measurements [85]. Production yields were then identified for abundant isotopes, both projectile-like fragments (PLFs) and target-like fragments (TLFs), automatically covering the whole angular range, and from various origins, not only deep-inelastic collisions but also fragments of transfer-induced fission. The comparison between the measurements and the calculations thus sheds light on the applicability of theoretical approaches. It is shown clearly that the SMF approach provides much better description for many-nucleon transfer processes, where TDHF fails to describe magnitude of production cross sections by orders of magnitude. Finally, the possibility to produce neutron-rich nuclei along the neutron magic number  $N = 126$  is discussed.

The article is organized as follows. In Sec. II, the theoretical frameworks of TDHF and the quantal diffusion approach for multinucleon transfer processes based on the SMF theory are recalled. In Sec. III, we present the results of TDHF and SMF calculations for the  $^{58,64}\text{Ni}+^{208}\text{Pb}$  reactions, which are compared with the available experimental data. Conclusions are given in Sec. IV.

## II. METHODS

### A. The TDHF theory

The TDHF theory in nuclear physics has a long history since the 1970s [87]. With the continuous development of computational technology, it has become a standard tool to investigate various nuclear dynamics microscopically within the self-consistent mean-field picture. It is nowadays regarded as a time-dependent energy density functional (TD-

EDF) approach rooted with the concept of nuclear density functional theory (DFT) and its time-dependent extension (TDDFT) [88]. With the use of a local EDF, the TDHF equation has a generic form:

$$i\hbar \frac{\partial \phi_h^q(\mathbf{r}\sigma, t)}{\partial t} = \sum_{\sigma'} \hat{h}_{\sigma\sigma'}^q(\mathbf{r}, t) \phi_h^q(\mathbf{r}\sigma', t), \quad (1)$$

where  $\phi_h^q(\mathbf{r}\sigma, t)$  are the  $h$ th occupied (hole) state with spatial, spin, and isospin coordinates,  $\mathbf{r}$ ,  $\sigma$ , and  $q$  ( $q = n$  for neutrons and  $q = p$  for protons), respectively.  $\hat{h}_{\sigma\sigma'}^q(\mathbf{r}, t)$  denotes the single-particle Hamiltonian which depends on various densities. For instance, the number and the current densities are expressed in terms of the single-particle orbitals as follows:

$$\rho_q(\mathbf{r}, t) = \sum_{h,\sigma}^{\text{occ.}} |\phi_h^q(\mathbf{r}\sigma, t)|^2, \quad (2)$$

$$\mathbf{j}_q(\mathbf{r}, t) = \frac{\hbar}{m} \sum_{h,\sigma}^{\text{occ.}} \text{Im}[\phi_h^{q*}(\mathbf{r}\sigma, t) \nabla \phi_h^q(\mathbf{r}\sigma, t)]. \quad (3)$$

EDF is constructed so as to reproduce static properties of finite nuclei over a wide range in the nuclear chart and basic nuclear matter properties in the spirit of nuclear DFT. With the use of the same form of EDF for static and dynamic calculations (disregarding possible memory effects in the functional), the TDHF approach offers a unified description of nuclear structure and dynamics without empirical parameters.

We note that the Pauli exclusion principle is automatically ensured for all times. With the spin-orbit interaction, the shell effects and deformation, both static and dynamic, are automatically described in a unified way. It is therefore possible to self-consistently describe complex reaction dynamics not only nucleon transfer, but also shape deformation (neck formation), surface vibrations, single-particle excitations, energy and angular momentum dissipation, microscopically from nucleonic degrees of freedom. The application of the TDHF approach ranges from collective excitation modes of an isolated nucleus [89–97] to nuclear reactions like transfer [37–49, 98–101], quasifission [50, 102–111], fusion [112–119], and fission [120–125]. For more details of the TDHF approach and its various applications, see, e.g., Refs. [34, 36, 87, 88, 126–128]. In this way, the TDHF approach is a versatile tool for studying quantum many-body dynamics in nuclear systems at low energies. However, the inherent suppression of fluctuations by the common mean-field needs to be overcome. The aim of the present paper is to tackle this problem by the SMF approach.

### B. The SMF theory

We recall the basic concepts inherent in the SMF approach. We will omit here the spin and isospin indexes for simplicity. For a detailed derivation and discussions, we refer the readers to, e.g., Refs. [57, 60, 69].

In low-energy heavy-ion reactions at energies around the Coulomb barrier, two-body dissipation would play a minor

role owing to the Pauli exclusion principle, and one-body dissipation presumably plays a predominant role. The observed agreements between recent TDHF calculations and experimental data offer strong support on this picture (see, e.g., Refs. [42, 55, 104]). It is therefore reasonable to assume that one-body (mean-field) fluctuations, the counterpart of the one-body dissipation, are the major source for generating a distribution of observables in nuclear reactions at low energies. Generally, the ground-state wave function of an atomic nucleus is not a mere single Slater determinant, but rather a superposition of many Slater determinants, as shown in, e.g., the success of the generator coordinate method (GCM) for nuclear structure calculations [129, 130], that can be viewed as quantal zero-point fluctuations of the mean-field potential.

To take into account the mean-field fluctuations, Ayik proposed [57] to introduce fluctuations in the density matrix at the initial time,

$$\rho^\lambda(\mathbf{r}, \mathbf{r}', t_0) = \sum_{i,j} \phi_i^*(\mathbf{r}, t_0) \rho_{ij}^\lambda \phi_j(\mathbf{r}', t_0), \quad (4)$$

where  $\lambda$  labels each stochastically-generated event. Note that the stochastic elements  $\rho_{ij}^\lambda$  in the right hand side of Eq. (4) do not depend on time. The generated density matrices evolve in time independently from each other according to its own self-consistent mean-field potential, i.e.:

$$i\hbar \frac{d\rho^\lambda}{dt} = [h[\rho^\lambda(t)], \rho^\lambda]. \quad (5)$$

Note that in the SMF approach the stochasticity is introduced only at the initial time, and the time evolution of the mean-field in each event  $\lambda$  itself is not a stochastic process. The key question, and this is the most important element behind the SMF theory, is how to imprint the initial fluctuations.

The initial fluctuations are introduced in the following way. Each event  $\lambda$  generates the expectation value of a one-body observable,  $\langle A \rangle^\lambda = \text{Tr}[\rho^\lambda A]$ . In the SMF approach, the original quantum mechanical framework is then replaced with a statistical treatment. Namely, the expectation value and the variance of a one-body observable are, respectively, evaluated as [131]

$$\overline{\langle A \rangle^\lambda} = \text{Tr}[\overline{\rho^\lambda} A] = \sum_{ij} \overline{\rho_{ij}^\lambda} A_{ji}, \quad (6)$$

$$\overline{(\langle A \rangle^\lambda - \overline{\langle A \rangle^\lambda})^2} = \overline{(\text{Tr}[\delta\rho^\lambda A])^2} = \sum_{ijkl} \overline{\delta\rho_{ij}^\lambda \delta\rho_{kl}^\lambda} A_{ji} A_{lk}, \quad (7)$$

where  $\delta\rho^\lambda$  is the fluctuating part of the density matrix, i.e.  $\delta\rho^\lambda = \rho^\lambda - \overline{\rho^\lambda}$ . Here and henceforth, the bar over quantities represents the ensemble average over the stochastically generated events. On the other hand, for the natural basis satisfying  $\langle i|\rho|j \rangle = n_i \delta_{ij}$  at the initial time, where  $n_i$  are average occupation numbers of the single-particle states, the quantum mechanical expressions of the expectation value and the variance

of a one-body observable are, respectively, given by [131]

$$\langle A \rangle = \sum_i n_i A_{ii}, \quad (8)$$

$$\langle A^2 \rangle - \langle A \rangle^2 = \frac{1}{2} \sum_{ij} [n_i(1-n_j) + n_j(1-n_i)] A_{ji} A_{ij}. \quad (9)$$

The essential point of the SMF theory is that it is designed in such a way that the expectation value and the variance obtained with the statistical treatment, Eqs. (6) and (7), coincide with the quantum expressions, Eqs. (8) and (9), respectively, at the initial time. It is accomplished by setting the initial fluctuations according to [57]

$$\overline{\rho_{ij}^\lambda} = n_i \delta_{ij}, \quad (10)$$

$$\overline{\delta\rho_{ij}^\lambda \delta\rho_{kl}^\lambda} = \frac{1}{2} [n_i(1-n_j) + n_j(1-n_i)] \delta_{kj} \delta_{li}. \quad (11)$$

Since the fluctuating components of the density matrix have zero mean, by construction, an ensemble average of those events reproduces the ordinary mean-field (TDHF) result.

We note that when the initial state has zero temperature such as the ground state of projectile and target nuclei before collision, the average occupation numbers  $n_i$  are zero or one. If an observable is diagonal at the initial state,  $A_{ij} = A_i \delta_{ij}$ , such as particle number operators for the projectile and target, as seen in Eq. (9), the variance of such observables are strictly zero and therefore they do not exhibit fluctuations at the initial state. If the initial state has a finite temperature, in the case of induced fission of a compound nucleus for instance, the average values of the occupation numbers are determined by the Fermi-Dirac distribution.

As mentioned in the introduction, it is worth noting here that, although the SMF approach was originally proposed to take into account one-body (mean-field) fluctuations at the initial time, it has been shown that it grasps part of many-body correlations through a simplified BBGKY hierarchy [59]. In addition, in the original formulation of the SMF approach [57], the stochastic matrix elements  $\delta\rho_{ij}^\lambda$  are assumed to be uncorrelated Gaussian random numbers with zero mean. Recently, in Ref. [131], by analyzing higher-order moments of one-body observables (the first and the second moments correspond to the mean and the variance, respectively), it has been shown that the description can be further improved by relaxing the Gaussian assumption (see also Ref. [132]). In the present article, however, we adopt the Gaussian assumption for the stochastic matrix elements, which allow us to formulate a quantal diffusion description for multinucleon exchanges, as described in Sec. II C. We leave further improvements of such model ingredients as future works.

### C. The quantal diffusion description

When dinuclear structure is maintained during a collision (cf. Fig. 1), it is possible to define a window at the neck region and derive quantal diffusion descriptions for multinucleon exchanges. Namely, it allows us to define neutron and proton

numbers of a projectile-like subsystem,  $N_1^\lambda(t)$  and  $Z_1^\lambda(t)$ , respectively, as macroscopic variables. Then, the nucleon exchange can be described as a diffusion process [133]. The evolution of the neutron and proton numbers is described by the Langevin equation:

$$\frac{d}{dt} \begin{pmatrix} N_1^\lambda(t) \\ Z_1^\lambda(t) \end{pmatrix} = \int g(x') \begin{pmatrix} \hat{e} \cdot \mathbf{j}_n^\lambda(\mathbf{r}, t) \\ \hat{e} \cdot \mathbf{j}_p^\lambda(\mathbf{r}, t) \end{pmatrix} d\mathbf{r} = \begin{pmatrix} \nu_n^\lambda(t) \\ \nu_p^\lambda(t) \end{pmatrix}, \quad (12)$$

where  $\mathbf{j}_q^\lambda(t)$  and  $\nu_q^\lambda(t)$  ( $q = n$  or  $p$ ) are the current densities and drift coefficients in the event  $\lambda$ , respectively. The unit vector  $\hat{e}$  is perpendicular to the window plane and directed along the relative position vector from the center of the target-like subsystem to the center of the projectile-like subsystem,  $\hat{e}(t) = \cos \theta(t) \hat{x} + \sin \theta(t) \hat{y}$ . Here,  $\theta(t)$  represents the (initially) smaller angle between the elongation axis of the colliding system and the collision axis. The elongation axis and the rotation angle  $\theta(t)$  can be determined by diagonalizing the mass quadrupole matrix as described in Refs. [64, 69]. The smoothing function,  $g(x') = \frac{1}{\sqrt{2\pi\kappa}} \exp[-x'^2/2\kappa^2]$ , extracts the contribution at the vicinity of the window plane, where  $x' = \hat{e} \cdot (\mathbf{r} - \mathbf{r}_0)$  with  $\mathbf{r}_0$  indicating the center of the window plane. The smoothing parameter  $\kappa = 1.0$  fm is used, which is the same order of the lattice spacing, as described in Ref. [67].

To obtain equations for the variances and the covariance, we use the stochastic part of the Langevin equation (12), which is linearized assuming small fluctuations around the mean evolution:

$$\frac{d}{dt} \begin{pmatrix} \delta N_1^\lambda(t) \\ \delta Z_1^\lambda(t) \end{pmatrix} = \begin{pmatrix} \frac{\partial \nu_n}{\partial Z_1} \delta Z_1^\lambda(t) + \frac{\partial \nu_n}{\partial N_1} \delta N_1^\lambda(t) \\ \frac{\partial \nu_p}{\partial Z_1} \delta Z_1^\lambda(t) + \frac{\partial \nu_p}{\partial N_1} \delta N_1^\lambda(t) \end{pmatrix} + \begin{pmatrix} \delta \nu_n^\lambda(t) \\ \delta \nu_p^\lambda(t) \end{pmatrix}. \quad (13)$$

Here,  $\delta N_1^\lambda = N_1^\lambda - N_1$  and  $\delta Z_1^\lambda = Z_1^\lambda - Z_1$  denote the stochastic part of neutron and proton numbers of the projectile-like subsystem, respectively, with  $N_1 = \overline{N_1^\lambda}$  and  $Z_1 = \overline{Z_1^\lambda}$ . Similarly,  $\delta \nu_n^\lambda = \nu_n^\lambda - \nu_n$  and  $\delta \nu_p^\lambda = \nu_p^\lambda - \nu_p$  denote the stochastic parts of neutron and proton drift coefficients, respectively, with  $\nu_n = \overline{\nu_n^\lambda}$  and  $\nu_p = \overline{\nu_p^\lambda}$ . The derivatives of the drift coefficients are evaluated at the mean trajectory. Multiplying both sides of Eq. (13) by  $\delta N_1^\lambda$  and  $\delta Z_1^\lambda$  and taking the ensemble average, one can derive a set of coupled partial differential equations [65, 69]:

$$\frac{\partial \sigma_{NN}^2}{\partial t} = 2 \frac{\partial \nu_n}{\partial N_1} \sigma_{NN}^2 + 2 \frac{\partial \nu_n}{\partial Z_1} \sigma_{NZ}^2 + 2D_{NN}, \quad (14)$$

$$\frac{\partial \sigma_{ZZ}^2}{\partial t} = 2 \frac{\partial \nu_p}{\partial Z_1} \sigma_{ZZ}^2 + 2 \frac{\partial \nu_p}{\partial N_1} \sigma_{NZ}^2 + 2D_{ZZ}, \quad (15)$$

$$\frac{\partial \sigma_{NZ}^2}{\partial t} = \frac{\partial \nu_p}{\partial N_1} \sigma_{NN}^2 + \frac{\partial \nu_n}{\partial Z_1} \sigma_{ZZ}^2 + \left( \frac{\partial \nu_n}{\partial N_1} + \frac{\partial \nu_p}{\partial Z_1} \right) \sigma_{NZ}^2, \quad (16)$$

with the initial conditions  $\sigma_{NN} = \sigma_{ZZ} = \sigma_{NZ} = 0$  at  $t = 0$ . Note that the particle number is not fluctuating at the initial time.  $\sigma_{NN}^2 = \overline{(N_1^\lambda - \overline{N_1^\lambda})^2}$  and  $\sigma_{ZZ}^2 = \overline{(Z_1^\lambda - \overline{Z_1^\lambda})^2}$  are the variances of neutron and proton numbers, respectively, and  $\sigma_{NZ}^2 = \overline{(N_1^\lambda - \overline{N_1^\lambda})(Z_1^\lambda - \overline{Z_1^\lambda})}$  is the covariance (or the mixed variance) of neutron and proton numbers.  $D_{NN}$  and

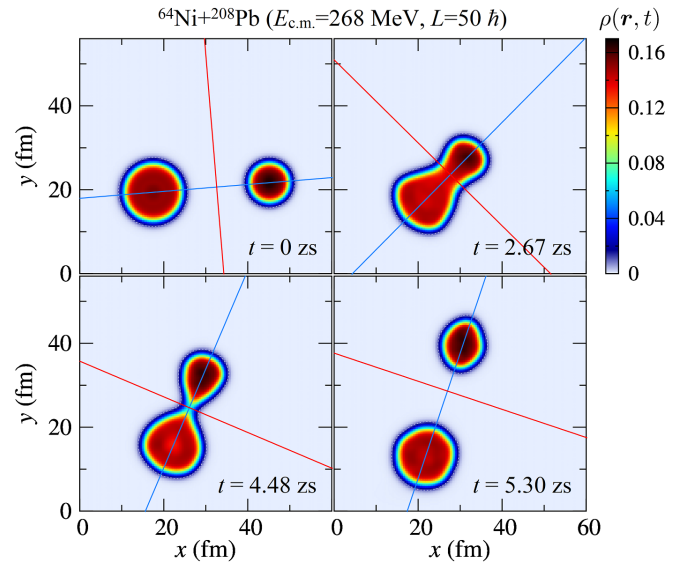


FIG. 1. Snapshots of density distribution in the  $^{64}\text{Ni}+^{208}\text{Pb}$  reaction at  $E_{c.m.} = 268$  MeV with  $L = 50\hbar$  are shown in the reaction plane. The blue line indicates the elongation axis which passes through the centers of mass of the projectile-like and target-like subsystems. The red line indicates the position of the window plane. A contour of  $\rho = 0.01 \text{ fm}^{-3}$  is indicated by dotted lines. Elapsed time is indicated in each panel in zeptoseconds ( $1 \text{ zs} = 10^{-21} \text{ s}$ ).

$D_{ZZ}$  are the quantal diffusion coefficients of neutron and proton exchanges, respectively. The same set of partial differential equations was employed in phenomenological nucleon exchange models for deep-inelastic collisions [134, 135]. It is worth emphasizing that all ingredients of Eqs. (14)–(16) are determined from the time evolution of the single-particle orbitals in TDHF, as described in Sec. II D. Therefore, it does not actually require us either to generate an ensemble of mean-field trajectories or to specify magnitude of fluctuations of  $\delta \rho_{ij}^\lambda$ . In practice, only a single TDHF calculation is sufficient to solve Eqs. (14)–(16), for a given set of initial conditions. Thus, a systematic investigation is feasible with moderate computational costs comparable to ordinary TDHF calculations.

#### D. Transport coefficients

To solve Eqs. (14)–(16), we need to have the drift and diffusion coefficients. While the mean drift coefficients,  $\nu_n$  and  $\nu_p$ , can be evaluated directly from the net mean currents [Eq. (3)] passing through the window in TDHF, it is not straightforward to take derivatives of them with respect to the neutron and proton numbers of the projectile-like subsystem [cf. Eqs. (14)–(16)]. We note that the Langevin equation (13) describes the evolution of macroscopic variables  $N_1$  and  $Z_1$  in the overdamped limit in which the inertial terms and the diffusion coefficients of the conjugate momentum of  $N_1$  and  $Z_1$  do not appear. To evaluate the derivatives of the drift coefficients, we

employ the Einstein relations in the over-damped limit,

$$\nu_n(t) = -\frac{D_{NN}(t)}{T^*} \frac{\partial}{\partial N_1} U(N_1, Z_1), \quad (17)$$

$$\nu_p(t) = -\frac{D_{ZZ}(t)}{T^*} \frac{\partial}{\partial Z_1} U(N_1, Z_1), \quad (18)$$

where  $T^*$  denotes the effective temperature and  $U(N_1, Z_1)$  is the potential energy surface of the colliding dinuclear system. The quantities  $D_{NN}$  and  $D_{ZZ}$  are the diffusion coefficients of the macroscopic variables  $N_1$  and  $Z_1$ , not of the conjugate momentum variables. The effective temperature was introduced by Randrup in Ref. [133]; see also Ref. [136]. In calculations of the derivative of drift coefficients, we do not need an explicit expression of the effective temperature. Only ratios of the curvature parameters and the effective temperature appear in Eqs. (17) and (18). It is possible to calculate these ratios, which are referred to as the reduced curvature parameters,  $\alpha = a/T^*$  and  $\beta = b/T^*$ , in terms of the mean drift path of the collision. The details of determination of the driving potential and the derivatives of the mean drift coefficients are given in Appendix A.

The diffusion coefficient is related to the auto-correlation function of the stochastic part of the drift coefficients,  $\delta\nu_q^\lambda$  [137, 138]:

$$D_{qq}(t) = \int_0^t \overline{\delta\nu_q^\lambda(t) \delta\nu_q^\lambda(t')} dt', \quad (19)$$

where

$$\begin{aligned} \delta\nu_q^\lambda(t) &= \hat{e} \cdot \frac{\hbar}{m} \sum_{i,j} \int d\mathbf{r} g(x') \\ &\times \text{Im}[\phi_i^{q*}(\mathbf{r}, t; \lambda) \nabla \phi_j^q(\mathbf{r}, t; \lambda)] \delta\rho_{ij}^\lambda. \end{aligned} \quad (20)$$

Note that the summation over  $i$  and  $j$  in Eq. (20) is taken for all the complete set of single-particle orbitals including unoccupied (particle) states.

By using the main postulate of the SMF approach, Eq. (11), together with the completeness relation in the diabatic approximation, it is possible to eliminate the unoccupied states from the expression [67]. As a result, the diffusion coefficients, including memory (non-Markovian) effects, are determined entirely by the occupied states in TDHF and are given by [67, 69]

$$\begin{aligned} D_{qq}(t) &= \int_0^t d\tau \int d\mathbf{r} \tilde{g}(x') \left( G_T(\tau) J_T^q(\mathbf{r}, t - \frac{\tau}{2}) \right. \\ &\quad \left. + G_P(\tau) J_P^q(\mathbf{r}, t - \frac{\tau}{2}) \right) \\ &- \int_0^t d\tau \text{Re} \left[ \sum_{h' \in \text{P}, h \in \text{T}}^{\text{occ.}} A_{h'h}^q(t) A_{h'h}^{q*}(t - \tau) \right. \\ &\quad \left. + \sum_{h' \in \text{T}, h \in \text{P}}^{\text{occ.}} A_{h'h}^q(t) A_{h'h}^{q*}(t - \tau) \right], \end{aligned} \quad (21)$$

where  $\tilde{g}(x') = \frac{1}{\sqrt{\pi\kappa'}} \exp[-(x'/\kappa')^2]$  is another smoothing function with a dispersion  $\kappa' = 0.5$  fm.  $G_{\text{P(T)}}(\tau) = \frac{1}{\sqrt{4\pi\tau_0}} \exp[-(\tau/2\tau_0)^2]$  is the averaged memory kernel for hole states. The memory time is given by  $\tau_0 = \kappa'/|u_0|$ , where

$u_0$  stands for the average flow speed of hole states across the window.  $J_\mu^q$  denotes the sum of magnitude of the current densities perpendicular to the window plane, whose contribution comes only from hole states which initially belong to either projectile ( $\mu = \text{P}$ ) or target ( $\mu = \text{T}$ ), i.e.,

$$J_\mu^q(\mathbf{r}, t) = \frac{\hbar}{m} \sum_{h \in \mu}^{\text{occ.}} \left| \hat{e} \cdot \text{Im}[\phi_h^{q*}(\mathbf{r}, t) \nabla \phi_h^q(\mathbf{r}, t)] \right|. \quad (22)$$

The hole-hole matrix elements,  $A_{h'h}^q(t)$ , are given by

$$\begin{aligned} A_{h'h}^q(t) &= \hat{e} \cdot \frac{\hbar}{2m} \int d\mathbf{r} g(x') \\ &\times \left( \phi_{h'}^{q*}(\mathbf{r}, t) \nabla \phi_h^q(\mathbf{r}, t) - \phi_h^{q*}(\mathbf{r}, t) \nabla \phi_{h'}^q(\mathbf{r}, t) \right). \end{aligned} \quad (23)$$

(See, Refs. [67, 69], for more details.)

The first term in the quantal diffusion coefficient (21) represents the sum of the nucleon currents between two subsystems across the window, which is integrated over the memory. It resembles the diffusion coefficient in the random walk problem, which is given by the sum of the rate for forward and backward steps [133, 137, 138]. On the other hand, the second term represents the Pauli blocking effect in nucleon transfer processes, which does not have a classical counterpart. In this way, the diffusion coefficients, which govern the fluctuation mechanism of the collective motion, can be determined entirely from the occupied single-particle orbitals in TDHF. It is rational because the one-body dissipation mechanism does present within the TDHF approach, which is related to the fluctuation mechanism as stated in the fluctuation-dissipation theorem.

## E. Primary production cross sections

To evaluate production cross sections, we need to compute the probability for production of each isotope. Within the TDHF approach, one can employ the particle-number projection method to obtain the probability to find  $n$  nucleons in a reaction product [37, 38],

$$P_n^{(q)}(b) = \frac{1}{2\pi} \int_0^{2\pi} e^{in\theta} \det\{\langle \phi_i^q | e^{-i\hat{N}_1^{(q)}\theta} | \phi_j^q \rangle\} d\theta, \quad (24)$$

where  $\hat{N}_1^{(q)}$  denotes the number operator for neutrons ( $q = n$ ) or protons ( $q = p$ ) in a fragment 1 and  $b$  is the impact parameter. The probability distribution,  $P_{N,Z}(b)$ , for the production of nuclei specified by  $(N, Z)$  has a product form,

$$P_{N,Z}^{\text{TDHF}}(b) = P_N^{(n)}(b) P_Z^{(p)}(b). \quad (25)$$

Therefore, there is essentially no correlation between neutron and proton transfers beyond mean-field (meaning that, e.g., neutrons and protons can still transfer in the same direction via shape evolution) in the TDHF approach. In other words, the covariance,  $\sigma_{NZ}^2 = \langle \hat{N}_1^{(n)} \hat{N}_1^{(p)} \rangle - \langle \hat{N}_1^{(n)} \rangle \langle \hat{N}_1^{(p)} \rangle$ , is strictly zero in TDHF, by construction. As already mentioned in the introduction, the particle-number projection method is merely

a way to extract the probabilities from the TDHF wave function after collision [37, 38]. Thus, it misses correlations between neutron and proton transfers and underestimates the widths of neutron and proton number distributions.

In the SMF approach, by solving the set of quantal diffusion equations, Eqs. (14)–(16), we can obtain the variances and the covariance of neutron and proton numbers of reaction products. For uncorrelated Gaussian random numbers, it can be shown that the Langevin equation (12) is equivalent to the Fokker-Plank description for the probability distribution  $P_{N,Z}(b)$  [139]. In particular when the drift coefficients have linear dependence as in the present case of the linearized form of the Langevin equation, the probability distribution is determined by a correlated Gaussian function. By employing this equivalence, we can write down the probability distribution,  $P_{N,Z}(b)$ , as follows:

$$P_{N,Z}^{\text{SMF}}(b) = \frac{\exp[-C_{N,Z}(b)]}{2\pi\sigma_{NN}(b)\sigma_{ZZ}(b)\sqrt{1-\eta_b^2}}, \quad (26)$$

with

$$C_{N,Z}(b) = \frac{1}{2(1-\eta_b^2)} \left[ \left( \frac{N - \bar{N}_b}{\sigma_{NN}(b)} \right)^2 + \left( \frac{Z - \bar{Z}_b}{\sigma_{ZZ}(b)} \right)^2 - 2\eta_b \left( \frac{N - \bar{N}_b}{\sigma_{NN}(b)} \right) \left( \frac{Z - \bar{Z}_b}{\sigma_{ZZ}(b)} \right) \right], \quad (27)$$

where  $\eta_b$  is the correlation coefficient, defined by the ratio of the covariance to the product of neutron and proton dispersions, i.e.,  $\eta_b \equiv \sigma_{NZ}^2(b)/\sigma_{NN}(b)\sigma_{ZZ}(b)$ .  $\bar{N}_b$  and  $\bar{Z}_b$  denote, respectively, the mean neutron and proton numbers of the reaction product in TDHF.

The production cross sections for *primary* reaction products (i.e., just after the collision before deexcitation) are then evaluated by an integration over the impact parameter:

$$\sigma(N, Z) = 2\pi \int_{b_{\min}}^{b_{\max}} b P_{N,Z}(b) db, \quad (28)$$

where the minimum and the maximum values of the impact parameters,  $b_{\min}$  and  $b_{\max}$ , are chosen according to the angular coverage of the corresponding experiment. Note that after multinucleon transfer processes reaction products can be highly excited, and one must evaluate effects of secondary deexcitation processes to make a direct comparison with experimental data.

## F. Secondary production cross sections

For the evaluation of the production cross sections for *secondary* reaction products (i.e., after deexcitation via particle evaporation, fission, and  $\gamma$ -ray emissions), we employ a statistical model for compound-nucleus disintegration processes. To this end, we follow the strategy as in Ref. [39]. In Ref. [39], the average total excitation energy (the sum of excitation energies of a PLF and a TLF) was estimated by

$$E_{N,Z}^*(b) = E_{\text{c.m.}} - E_{\text{kin}}^\infty(b) + Q_{\text{gg}}(N, Z), \quad (29)$$

where  $Q_{\text{gg}}(N, Z)$  denotes the ground-to-ground  $Q$  value for the exit channel involving a nucleus specified by  $(N, Z)$ . Here,  $E_{\text{kin}}^\infty(b)$  denotes the asymptotic value of TKE of outgoing fragments for the average products in TDHF. The average total excitation energy is then distributed to PLFs and TLFs in an appropriate way. This prescription was also used by other authors [45–48].

However, in the present systems under study as discussed in Sec. III D, reaction products involve transfer of many (more than 10) protons due to the quantal diffusion mechanism. In such a case, the Coulomb potential at the scission configuration can be substantially different from that of the mean trajectory. To have a feeling of it, imagine that we have touching Ni and Pb nuclei at distance  $R = 1.2(A_{\text{P}}^{1/3} + A_{\text{T}}^{1/3}) \simeq 12$  fm, for which we have the Coulomb potential  $V_{\text{C}} \simeq 275.5$  MeV. If we exchange protons between those nuclei, keeping the  $R$  value unchanged, the Coulomb potential shall be  $V_{\text{C}}' = (Z_{\text{P}} + \Delta Z)(Z_{\text{T}} - \Delta Z)e^2/R$ , where  $\Delta Z$  denotes the number of exchanged protons. The difference,  $\Delta V_{\text{C}} = V_{\text{C}}' - V_{\text{C}}$ , becomes, e.g., +6.4 MeV (−6.6 MeV) for  $\Delta Z = +2$  (−2), ..., +52.8 MeV (−76.8 MeV) for  $\Delta Z = +10$  (−10), and so on. The increase (decrease) of the Coulomb potential results in increase (decrease) of TKE and, thus, the total excitation energy will be decreased (increased). This is a crude estimation, as the  $R$  value could be larger due to fragment deformation, but it suggests that the secondary cross sections may be affected.

Therefore, to grasp the possible energy change due to proton transfers, we modify the expression of the average total excitation energy as follows:

$$E_{N,Z}^*(b) = E_{\text{c.m.}} - E_{\text{kin}}^\infty(b) + Q_{\text{gg}}(N, Z) - \Delta V_{\text{C}}(b, Z). \quad (30)$$

Here, the additional Coulomb correction term is defined as

$$\Delta V_{\text{C}}(b, Z) = \frac{Z(Z_{\text{tot}} - Z) - \bar{Z}_1(b, t_c)\bar{Z}_2(b, t_c)}{R(b, t_c)} e^2, \quad (31)$$

where  $Z_{\text{tot}} = Z_{\text{P}} + Z_{\text{T}}$  is the total number of protons in the system.  $t_c$  is chosen in the following way: (1) When two nuclei touch in the course of collision,  $t_c$  is taken as the instance at which a dinuclear system splits, assuming that TKE is determined by the Coulomb potential at scission; (2) When two nuclei do not touch,  $t_c$  is taken as the instance at the turning point, assuming that the proton transfer occurs at the closest approach. Processes with a finite contact time [see, Sec. III A and Fig. 2(a)] are regarded as “touched.”  $\bar{Z}_\mu$  ( $\mu = 1, 2$ ) and  $R$  represent the average number of protons in respective fragments and the relative distance between them, respectively, at the time  $t_c$ . In this way, the excitation energy becomes effectively transfer channel dependent by  $Q_{\text{gg}}$  and  $\Delta V_{\text{C}}$ . The estimated average total excitation energy (30) is then distributed to reaction products proportional to their mass. We should keep in mind that non-equilibrium excitation energy division may be possible especially for asymmetric systems (see, e.g., Refs. [136, 140, 141]). With the average total angular momentum of each reaction product, secondary processes are simulated by a statistical compound-nucleus deexcitation model,

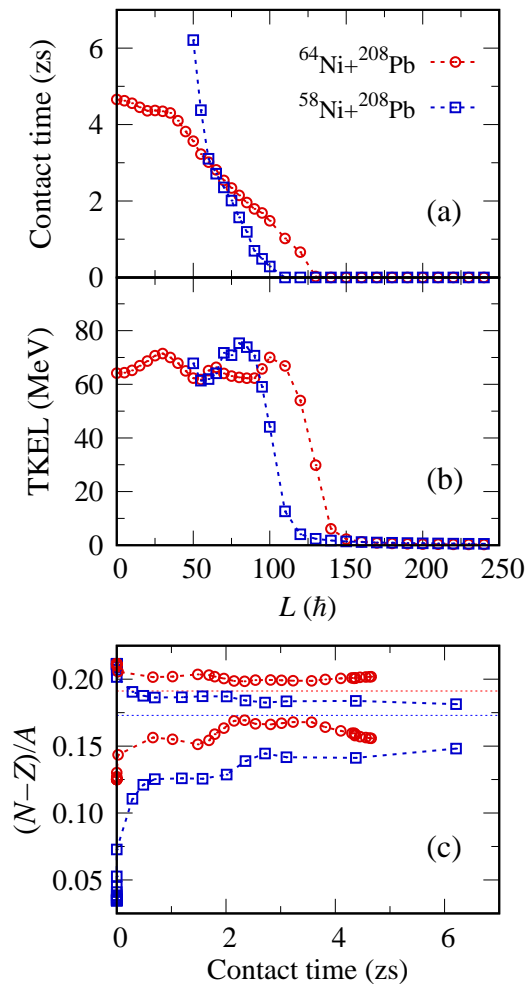


FIG. 2. Results of the TDHF calculations for the  $^{64}\text{Ni}+^{208}\text{Pb}$  reaction at  $E_{c.m.} = 268$  MeV (red open circles) and the  $^{58}\text{Ni}+^{208}\text{Pb}$  reaction at  $E_{c.m.} = 270$  MeV (blue open squares). In panels (a) and (b), contact time and average total kinetic energy loss (TKEL) are shown, respectively, as a function of the initial orbital angular momentum. In panel (c), average charge asymmetries,  $(N - Z)/A$ , for a PLF and a TLF are shown as a function of the contact time. The contact time is shown in zeptoseconds ( $1 \text{ zs} = 10^{-21} \text{ s}$ ).

GEMINI++ [142–144], which includes particle evaporation and fission in competition with  $\gamma$ -ray emission.

### G. Computational details

To perform the SMF calculations, three-dimensional (3D) parallel TDHF code [38] has been extended and applied. For the EDF, we employ the Skyrme SLy4d functional [145]. In the code, single-particle orbitals are represented on 3D uniform grid points with the isolated (box) boundary condition. The grid spacing is set to 0.8 fm. First and second spatial derivatives are computed with the 11-point finite-difference formulas. The Coulomb potential is computed by Fourier transforms. A computational box of  $24^3 \text{ fm}^3$  was used for the ground-state calculations, while a box of  $65 \times 60 \times 24 \text{ fm}^3$  was used for the reaction calculations. With this setting, we find

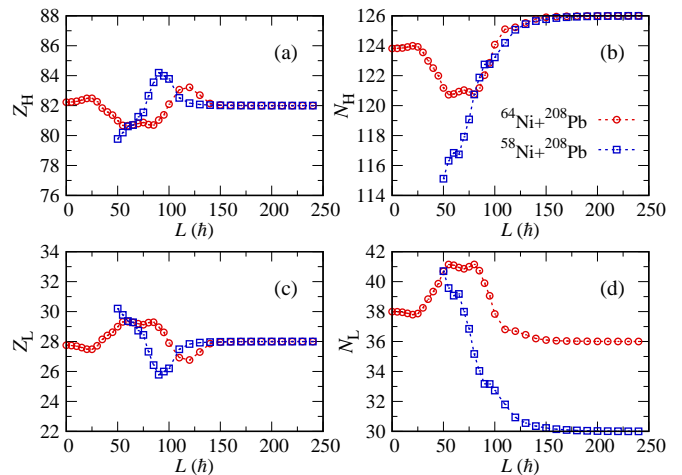


FIG. 3. Results of the TDHF calculations for the  $^{64}\text{Ni}+^{208}\text{Pb}$  reaction at  $E_{c.m.} = 268$  MeV (red open circles) and the  $^{58}\text{Ni}+^{208}\text{Pb}$  reaction at  $E_{c.m.} = 270$  MeV (blue open squares). In panels (a) and (b), average proton and neutron numbers of heavier (target-like) fragments,  $Z_H$  and  $N_H$ , are shown, respectively, as a function of the initial orbital angular momentum. In panels (c) and (d), those for lighter (projectile-like) fragments,  $Z_L$  and  $N_L$ , are shown.

that the ground state of  $^{58}\text{Ni}$  is of prolate shape with  $\beta = 0.12$ , while  $^{64}\text{Ni}$  exhibits a shape with  $\beta = 0.14$  with  $\gamma = 47^\circ$ .  $^{208}\text{Pb}$  is of course of spherical shape. We place those deformed projectiles to have an orientation with the smallest  $Q_{22}$  to be lying in the reaction plane. For the time evolution, the fourth-order Taylor expansion method was used with a single predictor-corrector step with  $\Delta t = 0.2 \text{ fm}/c$ . The initial separation distance between the projectile and target nuclei was set to 28 fm along the collision axis. The time evolution was stopped when the relative distance between PLF and TLF exceeds 28 fm.

To solve the quantal diffusion equations, we need to define the window plane which divides the colliding system into two parts. We place the window plane at the minimum density location along the elongation axis, as in Refs. [64, 65, 69, 71] (i.e., the window moves as a function of time). For a better detection of the minimum density, we first define  $\rho(x, y) = \int \rho(\mathbf{r}) dz$ , integrated over the axis perpendicular to the reaction plane, and then use the fifth-order polynomial interpolations for  $x$  and  $y$  directions. See Fig. 1, which depicts a typical example of the reaction dynamics, and also shows the window plane (indicated by a red line in each frame). To evaluate the neutron and proton numbers of the projectile-like subsystem,  $N_1(t)$  and  $Z_1(t)$ , a smooth step-like function,  $\Theta(x') = \frac{1}{2}[1 + \tanh(\alpha x'/\Delta x)]$ , is used, where  $|x'|$  is the distance from the window plane and  $\Delta x$  is the mesh spacing, with  $\alpha = 3$ . For the memory integral in the quantal diffusion coefficient, Eq. (21), we replace  $\int_0^t d\tau$  with  $\int_0^T d\tau$ , setting  $T = 0.33 \text{ zs}$ , which is sufficiently long to include possible memory effects on the diffusion process. We have confirmed that the memory effects in the first term of Eq. (21) can be well approximated with neglecting the memory time dependence of the currents, i.e., with  $\int_0^t G_\mu(\tau) d\tau \approx 1/2$ . The details of the determination of the curvature parameters for the driving potential in Eqs. (17) and (18) are given in Appendix A

For the particle-number projection method for TDHF



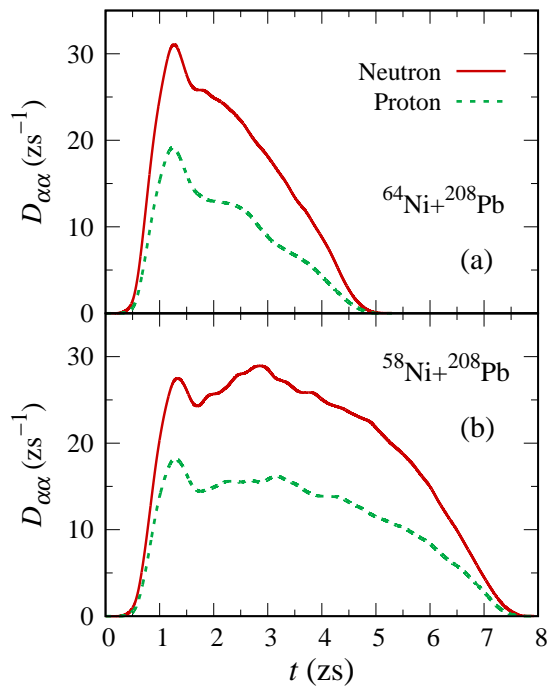


FIG. 4. Diffusion coefficients for neutron and proton transfers are shown as a function of time. Red solid line shows the diffusion coefficient for neutron transfer,  $D_{NN}(t)$ , while green dashed line shows that for proton transfer,  $D_{ZZ}(t)$ . In panels (a) and (b), results for the  $^{64}\text{Ni}+^{208}\text{Pb}$  reaction at  $E_{\text{c.m.}} = 268$  MeV and the  $^{58}\text{Ni}+^{208}\text{Pb}$  reaction at  $E_{\text{c.m.}} = 270$  MeV are presented, respectively. The initial orbital angular momentum is  $L = 50\hbar$  in both cases. Results were smoothed by taking an average over  $0.67$  zs (see texts).

[Eq. (25)], the interval  $[0, 2\pi]$  is discretized into 300 uniform grids. Since the experiments [85, 86] were carried out with thick targets and reaction products were identified by subsequent decay properties, the data should contain information of fragments in the whole angular range. To include all contributions for transfer products, we include impact parameters of  $b \lesssim 10$  fm, which correspond to the orbital angular momentum range up to  $L = 240\hbar$ , where  $L = b(2\mu E_{\text{c.m.}})^{1/2}$  (in units of  $\hbar$ ) with the reduced mass  $\mu$ . We mention here that for the  $^{64}\text{Ni}+^{208}\text{Pb}$  system with  $L < 30\hbar$  ( $b \lesssim 1$  fm) we observed an abrupt change of the minimum density location in the course of collision, which may be related to shell effects mentioned in Sec. III A. We thus excluded  $L < 30\hbar$  from the cross-section calculation, since it has little effect on the results. Also, for the  $^{58}\text{Ni}+^{208}\text{Pb}$  system with  $L = 45\hbar$ , we observed formation of binary products after a long contact time, about 25 zs. Since the contact time is rapidly increasing and the system is on the border between fusion and binary reactions,  $L = 45\hbar$  is not included in the cross-section calculation. GEMINI++ calculations were carried out with the default parameter set. We confirmed that the statistical treatment provides a convergent result.

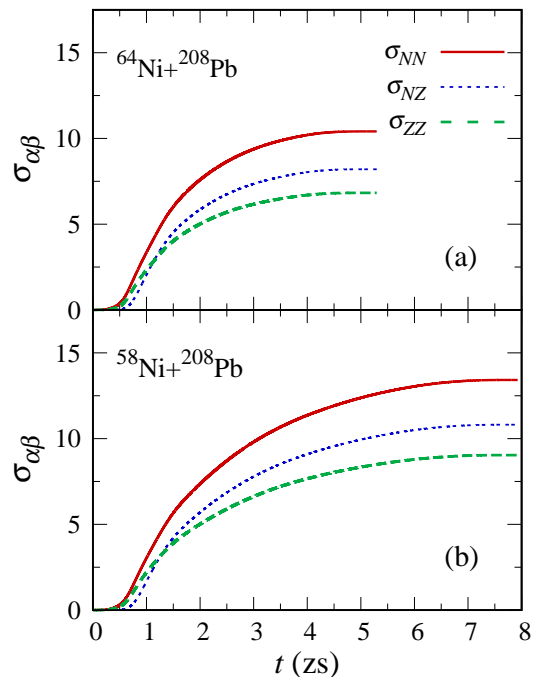


FIG. 5. Fluctuations and correlation for nucleon transfers are shown as a function of time. Red solid line shows the fluctuation in neutron transfer,  $\sigma_{NN}(t)$ , while green dashed line shows that in proton transfer,  $\sigma_{ZZ}(t)$ . By blue dotted line, the correlation between the neutron and proton transfers,  $\sigma_{NZ}(t)$ , is shown. In panels (a) and (b), results for the  $^{64}\text{Ni}+^{208}\text{Pb}$  reaction at  $E_{\text{c.m.}} = 268$  MeV and the  $^{58}\text{Ni}+^{208}\text{Pb}$  reaction at  $E_{\text{c.m.}} = 270$  MeV are presented, respectively. The initial orbital angular momentum is  $L = 50\hbar$  in both cases.

### III. RESULTS

#### A. Mean reaction dynamics in TDHF

We analyze the multinucleon transfer mechanism in the  $^{64}\text{Ni}+^{208}\text{Pb}$  reaction at  $E_{\text{c.m.}} = 268$  MeV and the  $^{58}\text{Ni}+^{208}\text{Pb}$  reaction at  $E_{\text{c.m.}} = 270$  MeV. Those collision energies correspond to  $E_{\text{c.m.}}/V_{\text{B}} \simeq 1.13$  and  $E_{\text{c.m.}}/V_{\text{B}} \simeq 1.09$  for the  $^{64}\text{Ni}+^{208}\text{Pb}$  and  $^{58}\text{Ni}+^{208}\text{Pb}$  systems, respectively, where  $V_{\text{B}}$  denotes the Coulomb barrier height estimated with the frozen Hartree-Fock method [146]. As a typical example of the reaction dynamics, time evolution of the density in the  $^{64}\text{Ni}+^{208}\text{Pb}$  reaction at  $E_{\text{c.m.}} = 268$  MeV with  $L = 50\hbar$  is shown in Fig. 1. Density contour plots at typical instances are shown in the reaction plane, where the elongation axis and the window plane are indicated as well. A great advantage of the TDHF approach is that it provides us intuitive information on the time evolution of nuclear dynamics, which is not a direct observable in experiments (See Ref. [147] for full movies of the reactions within the TDHF approach). In the course of the reaction, two nuclei collide deeply and then form a dinuclear structure connected with a thick neck (see,  $t = 2.67$  zs) that allows us to apply the quantal diffusion description for multinucleon transfers (cf. Sec. II C). A number of nucleons are exchanged between two subsystems through the window. After substantial diffusion of nucleon numbers, the dinuclear system eventually splits into two (see,  $t = 4.48$  zs). The well separated bi-

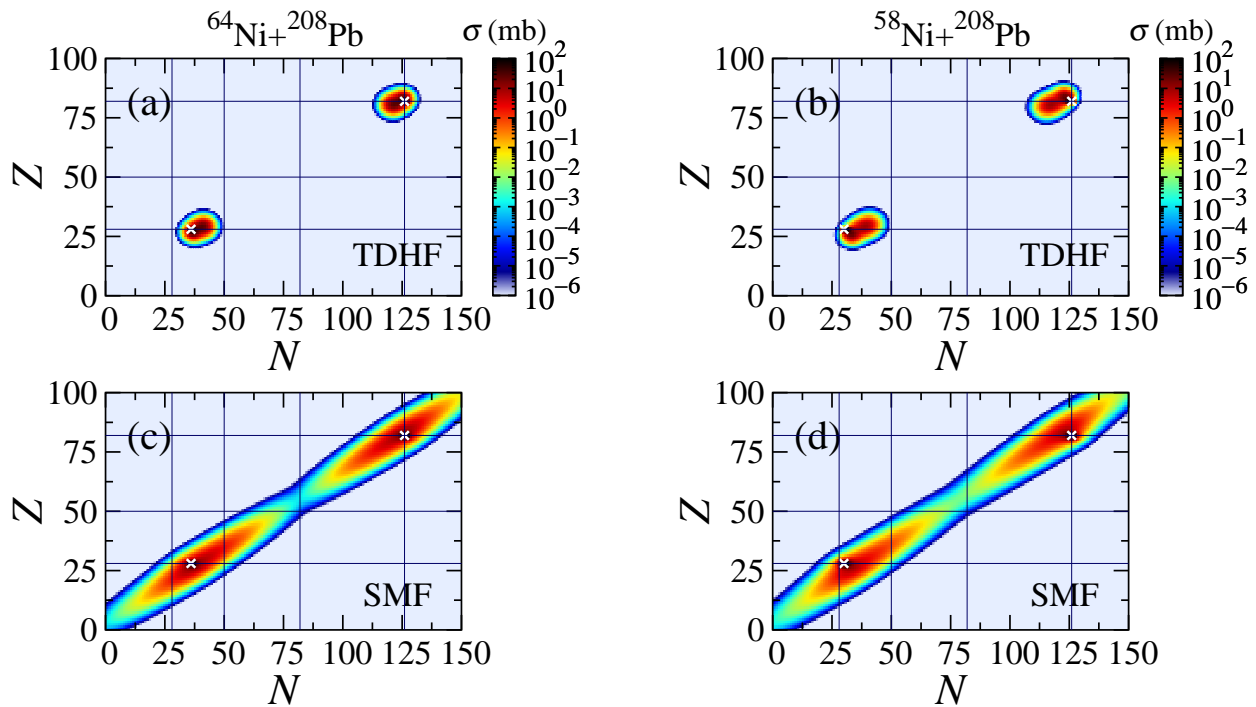


FIG. 6. Primary production cross sections for both light (projectile-like) and heavy (target-like) fragments are shown in the  $N$ - $Z$  plane for the  $^{64}\text{Ni}+^{208}\text{Pb}$  reaction at  $E_{c.m.} = 268$  MeV (left panels) and the  $^{58}\text{Ni}+^{208}\text{Pb}$  reaction at  $E_{c.m.} = 270$  MeV (right panels). Cross sections are shown in logarithmic scale in the units of millibarn. Upper panels [Figs. 6(a) and 6(b)] show the results of TDHF calculations, while lower panels [Figs. 6(c) and 6(d)] show the results obtained by the quantal diffusion approach based on the SMF theory. The horizontal lines indicate the proton magic numbers,  $Z = 28, 50,$  and  $82$ , while the vertical lines indicate the neutron magic numbers,  $N = 28, 50, 82,$  and  $126$ . The crosses point at the neutron and proton numbers of the projectile and target nuclei.

nary reaction products (see,  $t = 5.3$  zs) are then analyzed and various observables are calculated. Numerical results are presented in Tables I and II in Appendix B.

In Figs. 2 and 3, open circles show the results of TDHF calculations for the  $^{64}\text{Ni}+^{208}\text{Pb}$  reaction, while open squares show those for the  $^{58}\text{Ni}+^{208}\text{Pb}$  reaction. In Figs. 2(a) and 2(b), we show, respectively, the contact time and the average TKEL as a function of the initial orbital angular momentum. The contact time is defined as a duration during which the minimal density between colliding nuclei exceeds half the nuclear saturation density,  $\rho_{\text{sat}}/2 \simeq 0.08 \text{ fm}^{-3}$ . From the figure, we see a sharp increase of TKEL as the orbital angular momentum decreases, where the contact time becomes finite. In both collisions the maximum amount of TKEL is about 65–70 MeV, which occurs for the initial angular momentum less than  $L \leq 100\hbar$  for the  $^{64}\text{Ni}+^{208}\text{Pb}$  system and  $L \leq 90\hbar$  for the  $^{58}\text{Ni}+^{208}\text{Pb}$  system.

In Fig. 2(c), we show the mean values of the charge asymmetry of the primary PLF and TLF,  $\delta = (N - Z)/(N + Z)$ , as a function of the contact time. Note that each point corresponds to the result with different orbital angular momenta. The equilibrium values of the charge asymmetries of the composite dinuclear systems are  $\delta \simeq 0.19$  and  $0.17$ , for the  $^{64}\text{Ni}+^{208}\text{Pb}$  and  $^{58}\text{Ni}+^{208}\text{Pb}$  systems, respectively. These values are indicated by horizontal dotted lines in the figure. As can be seen from Fig. 2(c), a fast charge equilibration process takes place within about 1 zs. Then, the system evolves slowly toward the mass equilibrium, keeping the isospin asymmetry

roughly constant. Note that the systems do not reach the equilibrium values, because the systems do not reach the mass equilibrium as well. The saturated values of  $\delta$  correspond to the  $N/Z$  ratios of about 1.4 and 1.5 for PLF and TLF, respectively, in  $^{64}\text{Ni}+^{208}\text{Pb}$  and 1.46 for TLF in  $^{58}\text{Ni}+^{208}\text{Pb}$ , which are in good agreement with the experimentally deduced average  $N/Z$  ratios [85, 86].

To provide more detailed information on nucleon transfers, in Fig. (3), we show the average number of protons (left panels) and neutrons (right panels) in reaction products as a function of the initial orbital angular momentum. The upper panels [Figs. 3(a) and 3(b)] show those of heavier (target-like) fragments,  $Z_H$  and  $N_H$ , while the lower panels [Figs. 3(c) and 3(d)] show those of lighter (projectile-like) fragments,  $Z_L$  and  $N_L$ . For the quasielastic regime with large orbital angular momenta ( $L \gtrsim 150\hbar$ ), where TKEL and contact time are almost zero, the average neutron and proton numbers of the reaction products coincide with the initial values. As the orbital angular momentum decreases, two nuclei touche in the course of the collision and a rapid charge equilibration process takes place. At this stage, neutrons and protons are transferred toward the opposite directions as expected from the initial isospin asymmetries, that is,  $^{208}\text{Pb} \rightarrow ^{58,64}\text{Ni}$  for neutrons, and  $^{58,64}\text{Ni} \rightarrow ^{208}\text{Pb}$  for protons. The latter process is relatively fast, which occurs within 1 zs [cf. Fig. 2(a)], governed by nucleons around the Fermi level. As the orbital angular momentum decreases further, the dinuclear system starts evolving toward the mass symmetry. This trend is visible for

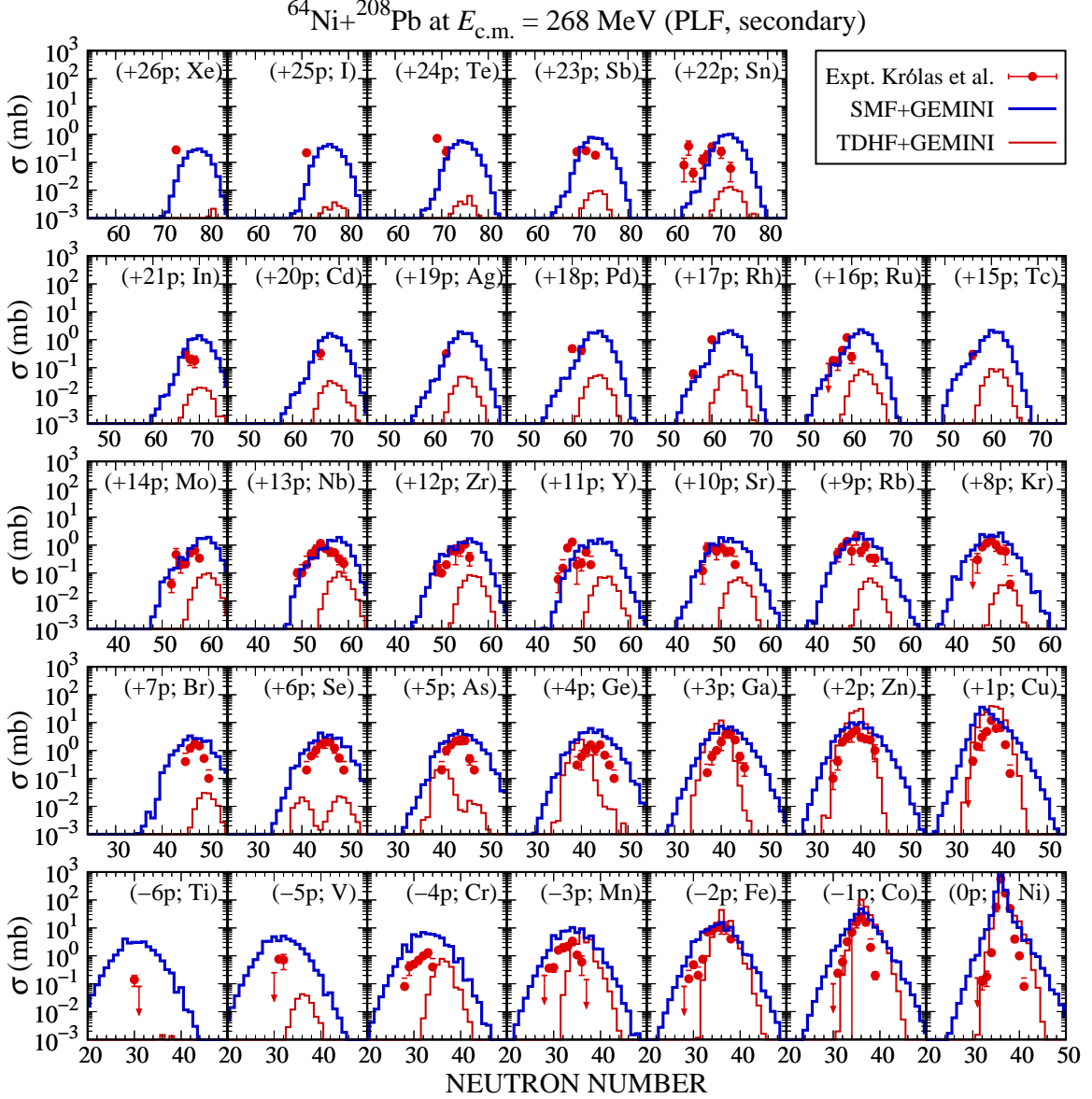


FIG. 7. Secondary production cross sections for lighter (projectile-like) fragments in the  $^{64}\text{Ni}+^{208}\text{Pb}$  reaction at  $E_{c.m.} = 268$  MeV. In each panel, production cross sections for different isotopes [as indicated by  $(\pm x p; X)$ , where  $x$  indicates the number of transferred protons and  $X$  stands for the corresponding element] are shown as a function of the neutron number. Blue thick histograms show the results of SMF+GEMINI calculations, while red thin histograms show those of TDHF+GEMINI. Red solid circles show the experimental data with error bars, taken from Ref. [85]. The down arrows indicate upper bound of the measured cross sections [85].

$80\hbar \lesssim L \lesssim 120\hbar$  and  $50\hbar \lesssim L \lesssim 90\hbar$  for the  $^{64}\text{Ni}+^{208}\text{Pb}$  and  $^{58}\text{Ni}+^{208}\text{Pb}$  systems, respectively. We find, however, that at small orbital angular momenta ( $L < 80\hbar$ ) the mass equilibration process is terminated in the  $^{64}\text{Ni}+^{208}\text{Pb}$  reaction. It is likely due to the shell effects around  $Z_H = 82$  and  $Z_L = 28$ , which are weakened by the fast isospin equilibration process in the  $^{58}\text{Ni}+^{208}\text{Pb}$  case. Notice that the contact time increases more rapidly for  $^{58}\text{Ni}+^{208}\text{Pb}$  as compared to  $^{64}\text{Ni}+^{208}\text{Pb}$  [see Fig. 2(a)], indicating that the former system favors to fuse. In fact, we observe fusion reactions for  $L \leq 40\hbar$  in the  $^{58}\text{Ni}+^{208}\text{Pb}$  reaction, where the system does not split for more than 40 zs, whereas no fusion was observed in the  $^{64}\text{Ni}+^{208}\text{Pb}$  reaction. (We mention here that in Ref. [38] the  $^{58}\text{Ni}+^{208}\text{Pb}$  reaction at slightly lower energy,

$E_{c.m.} = 257$  MeV, was investigated in TDHF and very similar reaction dynamics were observed.)

## B. Quantal diffusion for multinucleon transfers

In Fig. 4, we show the diffusion coefficients for neutron and proton transfers,  $D_{NN}(t)$  (solid line) and  $D_{ZZ}(t)$  (dashed line), respectively, as a function of time. The diffusion coefficients are evaluated according to Eq. (21), which are entirely determined by time evolution of the occupied single-particle orbitals in TDHF, as described in Sec. II D. To eliminate rapid oscillations due to complex dynamics of single-particle degrees of freedom including shell effects, the dif-

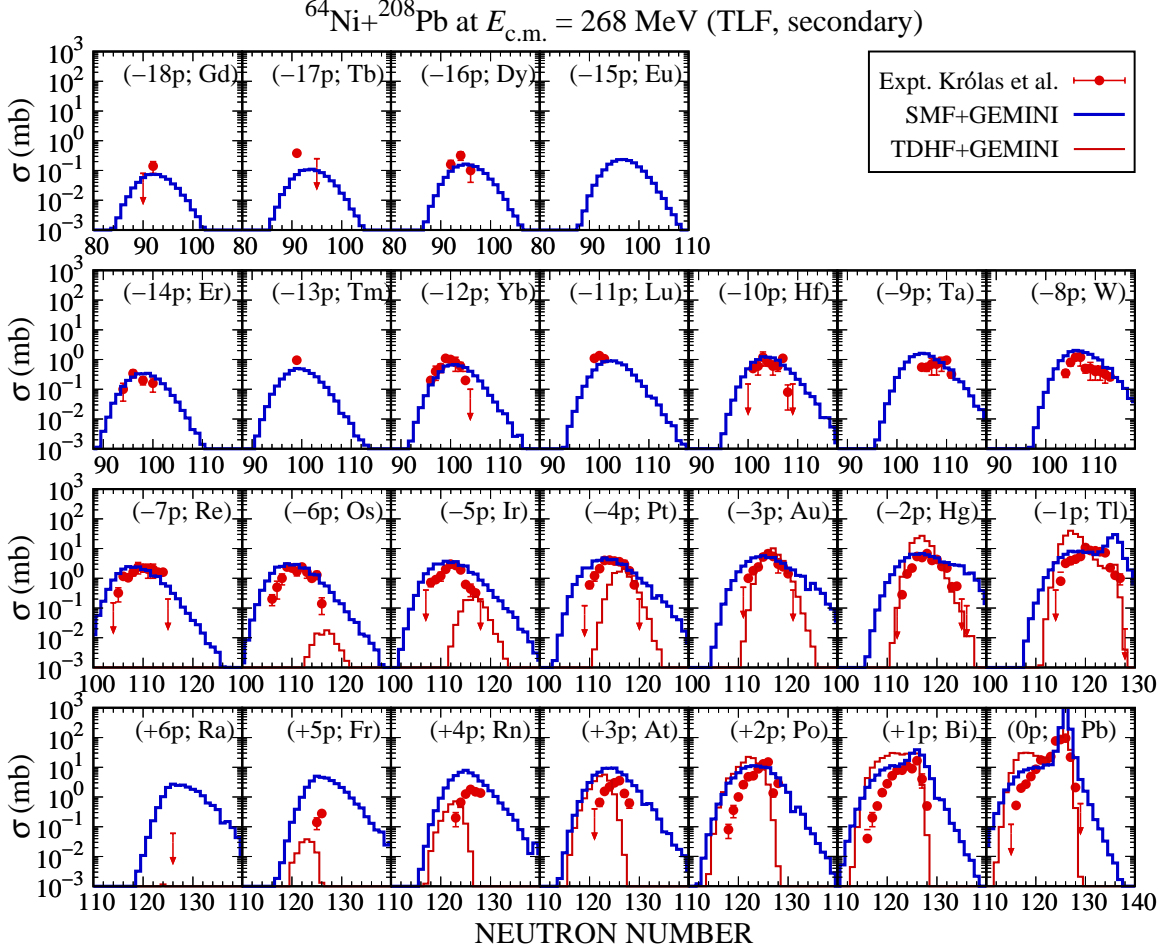


FIG. 8. Same as Fig. 7, but for heavier (target-like) fragments.

fusion coefficients are smoothed by taking an average over 0.67 zs, as in the case of the mean drift path described in Appendix A. In Figs. 4(a) and 4(b), the results for the  ${}^{64}\text{Ni}+{}^{208}\text{Pb}$  and  ${}^{58}\text{Ni}+{}^{208}\text{Pb}$  reactions are presented, respectively. The initial orbital angular momentum is  $L = 50\hbar$  for both cases (see Fig. 1 for the corresponding density plots in the  ${}^{64}\text{Ni}+{}^{208}\text{Pb}$  reaction). From the figure, it is clear that the diffusion coefficient for neutron transfers is systematically larger than that for protons, indicating influence of the Coulomb repulsion. In the initial stage of the reaction up to  $t \lesssim 1.5$  zs, both systems exhibit very similar behavior of the diffusion coefficients. The maximum values of the diffusion coefficients are around  $50 \text{ zs}^{-1}$  for neutrons and  $30 \text{ zs}^{-1}$  for protons. As mentioned above, the contact time is longer for the  ${}^{58}\text{Ni}+{}^{208}\text{Pb}$  system, in particular since  $L = 50\hbar$  is close to the border between fusion and binary events. As a result, the diffusion coefficients extend for a longer period for  ${}^{58}\text{Ni}+{}^{208}\text{Pb}$  [Fig. 4(b)] as compared to  ${}^{64}\text{Ni}+{}^{208}\text{Pb}$  [Fig. 4(a)].

In Fig. 5, the time evolution of the fluctuations and the correlation in neutron and proton transfers are shown as functions of time. Again, the results for the  ${}^{64}\text{Ni}+{}^{208}\text{Pb}$  and  ${}^{58}\text{Ni}+{}^{208}\text{Pb}$  reactions are shown in panels (a) and (b), respectively. The time evolution is obtained by solving the set of partial differential equations, Eqs. (14)–(16). In the initial stage of the reaction up to  $t \lesssim 1.25$  zs, we find that the magnitude orders as

$\sigma_{NZ} < \sigma_{ZZ} < \sigma_{NN}$ . As time evolves further, the correlation develops, changing the order as  $\sigma_{ZZ} < \sigma_{NZ} < \sigma_{NN}$ , indicating the importance of correlations after substantial energy dissipation [cf. Figs. 2(a) and 2(b)]. We note that the correlation  $\sigma_{NZ}$  is strictly zero within the TDHF approach. The magnitude of the fluctuations in SMF is much larger than that obtained in TDHF. For instance, in TDHF we find  $\sigma_{NN}^{\text{TDHF}} = 1.43$  and  $\sigma_{ZZ}^{\text{TDHF}} = 1.27$  for  ${}^{64}\text{Ni}+{}^{208}\text{Pb}$ , and  $\sigma_{NN}^{\text{TDHF}} = 1.58$  and  $\sigma_{ZZ}^{\text{TDHF}} = 1.38$  for  ${}^{58}\text{Ni}+{}^{208}\text{Pb}$ , at  $L = 50\hbar$ . Clearly, TDHF severely underestimates the magnitude of the fluctuations and the correlation in dissipative collisions.

### C. Primary production cross sections

In Fig. 6, we show the primary production cross sections  $\sigma(N, Z)$  in the  $N$ - $Z$  plane for the  ${}^{64}\text{Ni}+{}^{208}\text{Pb}$  reaction at  $E_{\text{c.m.}} = 268$  MeV (left panels) and the  ${}^{58}\text{Ni}+{}^{208}\text{Pb}$  reaction at  $E_{\text{c.m.}} = 270$  MeV (right panels). In the upper panels [Figs. 6(a) and 6(b)] the results of TDHF calculations are shown, while the lower panels [Figs. 6(c) and 6(d)] show the results obtained within the quantal diffusion approach. The figure clearly exhibits the fact that TDHF indeed provides quite narrow distributions in both systems. In stark contrast, the SMF approach, as a result of the quantal diffusion mech-

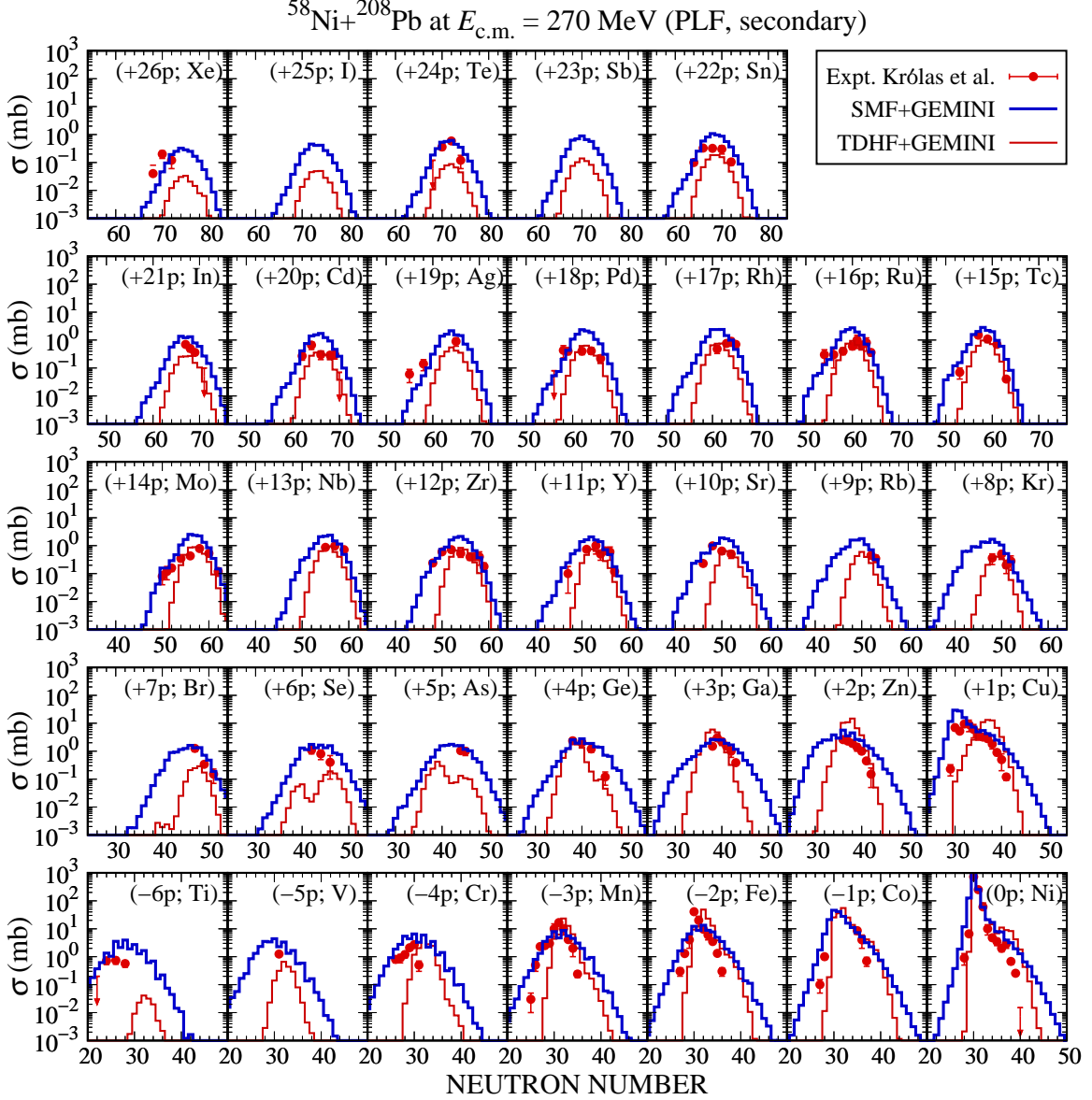


FIG. 9. Same as Fig. 7, but for the  $^{58}\text{Ni}+^{208}\text{Pb}$  reaction at  $E_{c.m.} = 270$  MeV. The experimental data were taken from Ref. [86].

anism, describes much broader distributions and therefore it predicts production of a large number of primary fragments in both systems. We note that the distributions in TDHF are nearly of round shape in the  $N$ - $Z$  plane, due to the product form of  $P_{N,Z}(b)$  [Eq. (25)] without correlations between neutron and proton transfers. The slightly skewed shape is due to the superposition of contributions from different impact parameters. On the other hand, in the SMF approach, neutron and proton transfers are substantially correlated, as indicated by a well-developed correlation  $\sigma_{NZ}$  in Fig. 5. As a result, the distributions in SMF exhibit a strongly correlated pattern which extends toward the mass symmetry of the system. The natural question is if such a very wide distribution is realistic. We shall answer in the next section by comparing the theoretical results with a full set of the experimental data reported by Królas *et al.* in Refs. [85, 86].

#### D. Secondary production cross sections

In Figs. 7 and 8, we show the secondary production cross sections for PLFs and TLFs, respectively, in the  $^{64}\text{Ni}+^{208}\text{Pb}$  reaction at  $E_{c.m.} = 268$  MeV and compare the results with the measured cross sections [85]. Similarly, in Figs. 9 and 10, we show the secondary production cross sections for PLFs and TLFs in the  $^{58}\text{Ni}+^{208}\text{Pb}$  reaction at  $E_{c.m.} = 270$  MeV, respectively, with the experimental data [86]. In those figures, the measured cross sections are shown by solid circles with error bars. Upper bound of the measured cross sections [85, 86] is also indicated by a down arrow when available. The results obtained by the quantal diffusion approach based on the SMF theory are shown by thick histograms, while the results of TDHF calculations are shown by thin histograms. Each panel shows the isotopic distribution as a function of the neutron number of the reaction product. The number of trans-

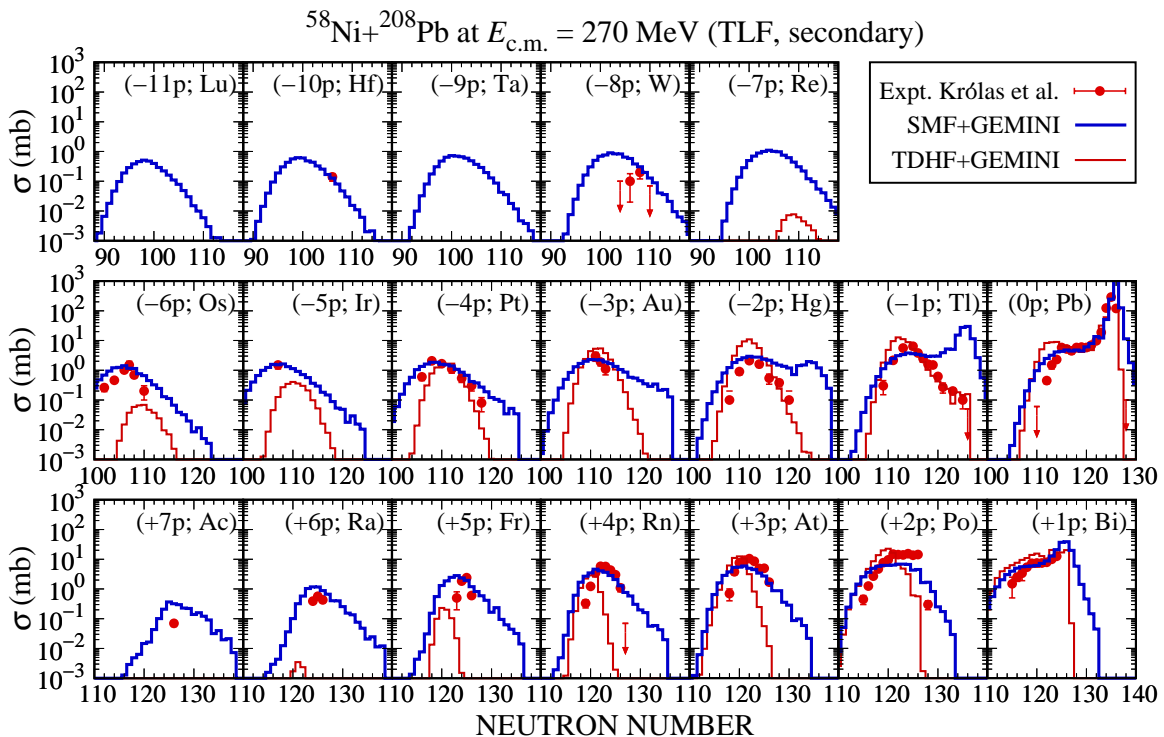


FIG. 10. Same as Fig. 9, but for heavier (target-like) fragments.

ferred protons and the corresponding element are indicated by  $(\pm xp, X)$ , where the sign indicates difference relative to the proton number of the projectile or the target and  $X$  stands for the corresponding element.

We start with a discussion on the TDHF results (red thin histograms, denoted by “TDHF+GEMINI” in the figures), which are expected to work well around the average values and do not include the correlation between neutron and proton transfers. First, we focus on the channels accompanying proton transfer from nickel to lead, corresponding to the direction of the isospin equilibration in the initial systems,  $^{58,64}\text{Ni}$  and  $^{208}\text{Pb}$  (the bottom row of the figures). The latter channels are mainly contributed from the fast charge equilibration process at peripheral (grazing) collisions [cf. Figs. 2 and 3]. This type of processes is ubiquitous in systems with relatively large isospin asymmetry (see, e.g., Refs. [38, 148–152]). From the figures, one can see that TDHF works fine when the number of transferred nucleons is small [e.g., (0p) channel with transfer of several neutrons, (-1p) and (-2p) channels with transfer of a few neutrons in Fig. 7]. However, as the number of transferred protons increases further [see, e.g., (-3p)–(-6p) channels in Fig. 7], TDHF substantially underestimates the magnitude of the production cross sections. Moreover, the peak position of the isotopic distributions for PLFs appears too neutron-rich [see, e.g., (-3p)–(-5p) channels in Fig. 7]. This trend was also observed for other systems [39], although it was not clear if this is due to underestimation of neutron evaporation effects or not. Interestingly, by looking at the corresponding proton-transfer channels for the heavier partner [i.e., (+3p)–(+5p) in Fig. 8], we find that the peak position of the isotopic distributions for TLFs appears too neutron-deficient. The combination of those two observations indicates that pro-

ton removal (addition) tends to accompany neutron removal (addition), implying the importance of the correlation in neutron and proton transfers.

Next, we discuss the TDHF results for channels accompanying transfer toward the direction of the mass symmetry. As discussed in Sec. III A, for small initial orbital angular momenta, an onset of quasifission emerges, where the system starts evolving toward the mass symmetry. The latter process corresponds to the proton pickup ( $+xp$ ) with respect to the projectile (Figs. 7 and 9) and to the proton removal ( $-xp$ ) with respect to the target (Figs. 8 and 10). Because of relatively short contact times, however, the system does not reach the mass equilibrium and we observed transfer of only two protons from Ni to Pb on average in TDHF [cf. Figs. 3(a) and 3(c)]. As a result, TDHF provides a good description for channels with transfer of a few protons from Ni to Pb, which are close to the average value [see, e.g., (+1p), (+2p), and (+3p) channels in Fig. 7 and (-1p), (-2p), and (-3p) channels in Fig. 8]. As the number of transferred protons increases further, however, TDHF substantially underestimates the magnitude of the production cross sections [see, e.g., (+4p)–(+7p) channels in Fig. 7 and (-4p)–(-7p) channels in Fig. 8]. Furthermore, the experimental data for PLFs (Figs. 7 and 9) exhibit considerable cross sections for channels with transfer of a number of protons, up to (+26p) channel. We find that the cross sections for those channels contain substantial contributions from transfer-induced fission of heavy partners. Comparing with the experimental data, the magnitude of those cross sections are underestimated for  $^{64}\text{Ni}+^{208}\text{Pb}$  (Fig. 7), while it is comparable to the data for  $^{58}\text{Ni}+^{208}\text{Pb}$  (Fig. 9). It indicates that the transfer-induced fission is reasonably simulated by GEMINI++. On the other hand, for the TLFs, TDHF

completely fails to reproduce the experimental data for the channels accompanying removal of many protons [see, e.g.,  $(-8p)$ – $(-18p)$  channels in Fig. 8]. This comparison clearly illustrates the usefulness and limitation of TDHF+GEMINI in describing multinucleon transfer processes in deep-inelastic collisions.

We shall now turn to a discussion on the results obtained by the quantal diffusion approach based on the SMF theory (blue thick histograms, denoted by “SMF+GEMINI” in the figures). As can be seen from Figs. 7–10, we find that the SMF approach provides a very good overall description of the measured production cross sections, all the way up to  $(+26p)$  channel for lighter fragments (Figs. 7 and 9) and  $(-18p)$  channel for heavier fragments (Fig. 8). Through an analysis of the data for PLFs [Figs. 7 and 9], we find that the production cross sections up to around  $(+14p)$  are dominated by the quantal diffusion mechanism. In contrast, the production cross sections for Tc ( $Z = 43$ ) to Xe ( $Z = 54$ ) isotopes [i.e.,  $(+15p)$ – $(+26p)$  channels in Figs. 7 and 9], we find a substantial contribution of transfer-induced fission of heavy partners. It is remarkable that the SMF approach reproduces transfers in both directions, owing to the quantal diffusion mechanism. The observed agreement between the SMF results and the measurements suggests that a proper description for the production of heavy nuclei and their subsequent decays is essential to reproduce the experimental data for the production of Tc to Xe isotopes.

We should point out, however, that the SMF approach overestimates the width of isotopic distributions, see, e.g., the bottom two rows of Figs. 7–10. We consider that this overestimation is associated with the linearization of the Langevin equation (12). In addition, there is disagreement with the experimental data, which is visible, for instance, in  $(-1p)$  channel for TLF in the  $^{64}\text{Ni}+^{208}\text{Pb}$  system shown in Fig. 8 and  $(-1p)$  and  $(-2p)$  channels for TLF in the  $^{58}\text{Ni}+^{208}\text{Pb}$  system shown in Fig. 10. Those channels are contributed by collisions with large orbital angular momenta. We consider that the probability distribution of the Gaussian form (26) is inappropriate for this regime, as indicated by transfer probabilities in TDHF [37, 38]. Indeed, for those channels TDHF correctly describes the shape of the isotopic distributions. It is actually possible to further improve the quantal diffusion description by incorporating nonlinear effects in the Langevin equation (12). Although we expect that the improved quantal diffusion description provides a better description of the experimental data presented in this work, we leave it as a future work.

For a complete representation of the data, we show in Fig. 11 mass distributions of secondary reaction products. In Fig. 11(a) and 11(b), the results for the  $^{64}\text{Ni}+^{208}\text{Pb}$  and  $^{58}\text{Ni}+^{208}\text{Pb}$  reactions are presented, respectively. The experimental data [85, 86] are shown by open circles with error bars, while solid lines represents the results of SMF+GEMINI calculations. The results of TDHF+GEMINI are also shown by thin dotted lines for comparison. We note that the data are merely an integration of the absolute cross sections shown in Figs. 7–10 for a given mass number  $A$  and do not involve any renormalization for comparison. We also note that the experimental data for the  $^{58}\text{Ni}+^{208}\text{Pb}$  reaction are less complete than the other, since the off-line radioactivity measure-

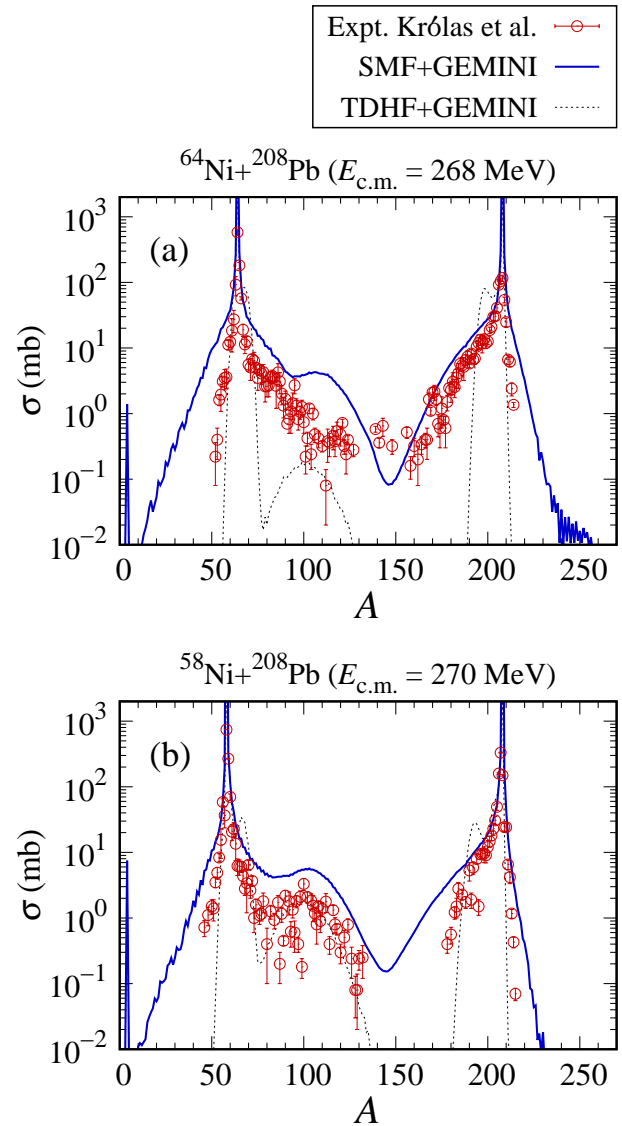


FIG. 11. Mass distributions for secondary reaction products. In panels (a) and (b), results for the  $^{64}\text{Ni}+^{208}\text{Pb}$  reaction at  $E_{c.m.} = 268$  MeV and the  $^{58}\text{Ni}+^{208}\text{Pb}$  reaction at  $E_{c.m.} = 270$  MeV are shown, respectively. The measured cross sections are shown by red open circles with error bars, which were taken from Refs. [85, 86]. Blue solid line represents the results of SMF+GEMINI calculations, while the results of TDHF+GEMINI calculations are indicated by a thin dotted line.

ment was not carried out for this system [86]. From the figure we find that the SMF approach provides much wider mass distributions as compared to the TDHF approach. A comparison with the SMF results and the measurements reveals that the SMF approach predicts somewhat wider distributions, which are larger in magnitude, as compared to the experimental data. The overestimation may partly be due to the linearization of the Langevin equation, as mentioned above. We note, however, that the experimental data points in Figs. 7–10 are limited in some regions, whereas the mass distributions in the SMF approach involve the entire cross sections for all isotopes, that would result in larger magnitude. We note that there is a sizable contribution of transfer-induced fission

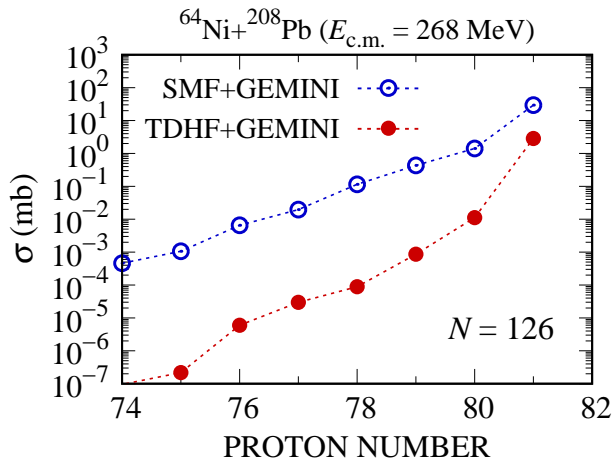


FIG. 12. Secondary production cross sections for  $N = 126$  isotones in the  $^{64}\text{Ni}+^{208}\text{Pb}$  reaction at  $E_{c.m.} = 268$  MeV are shown as a function of the proton number of the reaction products. Blue open circles represent the results of SMF+GEMINI calculations, while red solid circles represent those of TDHF+GEMINI.

around  $A \simeq 90$ – $140$  in both systems. We find a noticeable contribution of transfer-induced fission also in TDHF+GEMINI, while it is much bigger in SMF+GEMINI. Those fission products contribute to generate cross sections for Tc to Xe isotopes [i.e.,  $(+15p)$ – $(+26p)$  channels in Figs. 7 and 9], as mentioned above.

Finally, Fig. 12 illustrates the prediction of the secondary production cross sections for  $N = 126$  isotones in the  $^{64}\text{Ni}+^{208}\text{Pb}$  reaction at  $E_{c.m.} = 268$  MeV. In the figure, open and solid circles indicate the results of the SMF and TDHF calculations, respectively. The magnitude of the cross sections are closer for one-proton transfer, but the SMF approach predicts cross sections larger by several orders of magnitude with increased number of removed protons from lead. We mention here that the experimentally deduced cross sections for the  $N = 126$  isotones production in the  $^{136}\text{Xe}+^{198}\text{Pt}$  reaction [153] exhibit the magnitude which is comparable to (or even slightly larger than) that indicated by SMF+GEMINI for the present system. The figure highlights the necessity to go beyond the standard TDHF description for a quantitative prediction of production of unstable nuclei with neutron and proton numbers which are far apart from the average values.

#### IV. SUMMARY AND CONCLUSIONS

Recently, it has been hoped that the multinucleon transfer reaction in low-energy heavy-ion reactions may be an efficient mechanism for production of yet-unknown neutron-rich heavy nuclei and also for synthesizing neutron-rich superheavy elements. Aiming at the production of new neutron-rich nuclei, much experimental effort has been undertaken already that will be continued for the coming future. Several macroscopic or microscopic transport approaches have been developed for theoretical investigations of the multinucleon transfer mechanism [7]. These transport approaches are, in general, very useful for analyzing the experimental data. However, be-

cause of a number of adjustable parameters they involve, they have limited predictive power. The time-dependent Hartree-Fock (TDHF) approach provides a microscopic description for low-energy heavy-ion reactions. While the mean-field approach has been very successful for describing the most probable path of the collective motion, it severely underestimates the dynamical fluctuations and distributions of observables around their average values. Recently, as an extension of the TDHF approach, the time-dependent random phase approximation (TDRPA) has been applied to low-energy heavy-ion collisions. Since the TDRPA formula is obtained by linearizing the equation of motion around the mean evolution, it provides a good approximation for dispersion of one-body observables when amplitude of fluctuations is sufficiently small. However, this approach appears to have a technical problem in describing dispersions of one-body observables in asymmetric systems [55]. As seen from recent publications [69–73], the quantal diffusion description for multinucleon exchanges based on the stochastic mean-field (SMF) approach provides very good description for multinucleon transfer mechanism, which is applicable for asymmetric reactions as well.

In this work, we have applied the quantal diffusion approach based on the SMF theory to analyze the multinucleon transfer mechanism in the  $^{64}\text{Ni}+^{208}\text{Pb}$  reaction at  $E_{c.m.} = 268$  MeV and the  $^{58}\text{Ni}+^{208}\text{Pb}$  reaction at  $E_{c.m.} = 270$  MeV. The rich experimental data by Królas *et al.* [85, 86], which were measured with thick targets and therefore include both projectile-like and target-like fragments as well as transfer-induced fission products, allowed us to confirm the usefulness and limitations in the TDHF and the SMF approaches. In general, it turns out that the quantal diffusion approach provides very reasonable description of the experimental data, in both directions of transfers from projectile to target and vice versa, for both projectile-like and target-like fragments. A striking finding is a significant contribution of transfer-induced fission of heavy reaction products, which nicely agree with the experimental observation. In some cases the SMF calculations overestimate the isotopic widths, which may be due to the linear approximation employed in the Langevin equation for macroscopic variables. Based on the quantal diffusion approach, we have found that the production cross sections for  $N = 126$  isotones could be significantly larger than those expected within the TDHF approach [46–48]. It underlines the importance of going beyond, especially to include one-body (mean-field) fluctuations and correlations, the standard TDHF description for predicting production cross sections of unknown neutron-rich heavy nuclei.

With the SMF theory we have achieved a remarkable progress in microscopic description of low-energy heavy-ion reactions, as compared to the standard TDHF approach. Nevertheless, there still remains some room for further improvements of the theoretical framework. Below, we envision possible future directions:

1. *Nonlinear effects in the quantal diffusion mechanism.* As outlined in Sec. II C, in deriving the quantal diffusion description, we have linearized the Langevin equation (12) around the mean trajectory, assuming small



amplitude fluctuations. Note that a similar assumption is made in the TDRPA approach as well [35, 36, 53–56]. In addition, a simple parabolic form has been assumed for the driving potential  $U(N, Z)$  [cf. Eq. (A1)], and it can be generalized by introducing anharmonicity in the potential form. Such extensions are expected to reduce the isotopic width and would result in better agreement with the experimental data.

2. *TKE distributions.* So far, we have not discussed how to describe distributions of the collective relative motion, namely, fluctuations in scattering angles as well as total kinetic energy (TKE). The distribution of TKE is, in turn, related to the total excitation energy distribution as discussed in Sec. II F. In principle, one can adapt the SMF concept to the relative motion of a colliding system, which allows us to evaluate fluctuations of, e.g., TKE based on microscopic mean-field dynamics. A work is in progress along this line.
3. *Pairing correlations.* In the present work, we have neglected the pairing correlations, assuming that pairing in atomic nuclei is so fragile and plays a minor role in dissipative heavy-ion collisions. However, pairing may alter reaction dynamics in an unexpected way, as shown in, e.g., Refs. [154–158]. Actually, the SMF approach has already been generalized to include the pairing correlations [159]. With the recent developments of mean-field approaches including pairing for static properties [160–163] and dynamics [92, 154–158, 164–167], the application of the quantal diffusion approach is feasible, as outlined in this work.

Finally, we comment on the Gaussian assumption of the initial fluctuations in the density matrix,  $\delta\rho_{ij}^\lambda$ . In Refs. [131, 132], effects of relaxing of the Gaussian assumption have been explored. In particular, it has been shown that third- and fourth-order moments of a one-body observable can be better described by an appropriate relaxation [131]. We note, however, that the Gaussian assumption is used to formulate the quantal diffusion approach for multinucleon exchanges as described in Sec. II C. Thus, although it is possible to further improve the model ingredients for more realistic description including higher moments of one-body observables by relaxing the Gaussian assumption, it is then necessary to generate an ensemble of TDHF trajectories that requires vast computational costs. We also mention here that another possible extension has been proposed recently in Ref. [168], where the SMF concept is applied to the time-dependent reduced density matrix approach.

To conclude, in this work we have demonstrated that the quantal diffusion approach based on the SMF theory is a powerful and promising tool of choice to microscopically and quantitatively describe multinucleon transfer processes in low-energy heavy-ion reactions. We emphasize that the quantal diffusion approach based on the SMF theory does not involve any adjustable parameters, once an energy density functional is given, and transport coefficients are entirely determined from the occupied single-particle orbitals in the TDHF

approach. The observed agreement with the full set of the experimental data is not only remarkable, but also encouraging for microscopic mean-field theories for predicting and understanding various outcomes from complex many-body dynamics of low-energy heavy-ion reactions.

## ACKNOWLEDGMENTS

The authors thank Bülent Yilmaz of Ankara University for useful comments on the window dynamics. K.S. gratefully acknowledges Tennessee Technological University for partial financial support and hospitality during his visit. S.A. is very much thankful to his wife F. Ayik for continuous support and encouragement. This work is supported in part by U.S. Department of Energy (DOE) Grant No. de-sc0015513, and in part by JSPS Grant-in-Aid for Early-Career Scientists Grant No. 19K14704. This work used the computational resource of the HPCI system (Oakforest-PACS) provided by Joint Center for Advanced High Performance Computing (JCAHPC) through the HPCI System Project (Project ID: hp190002), and (in part) by Multidisciplinary Cooperative Research Program (MCRP) in Center for Computational Sciences (CCS), University of Tsukuba (Project ID: NUCLHIC). This work also used (in part) computational resources of the Cray XC40 System at Yukawa Institute for Theoretical Physics (YITP), Kyoto University.

## Appendix A: Derivatives of the mean drift coefficients

To solve the partial differential equations, Eqs. (14)–(16), one has to evaluate derivatives of the mean drift coefficients,  $\nu_n$  and  $\nu_p$ , with respect to the numbers of neutrons and protons in the projectile-like subsystem,  $N_1$  and  $Z_1$ . In the present article, we use the same strategy as in Refs. [65, 135, 169]. For completeness, we provide below the details of the procedure for the  $^{58,64}\text{Ni}+^{208}\text{Pb}$  reactions examined in the present paper.

### 1. For the $^{64}\text{Ni}+^{208}\text{Pb}$ system

From a TDHF calculation, one can compute time evolution of the mean neutron and proton numbers in the projectile-like subsystem,  $N_1(t)$  and  $Z_1(t)$ . Because of the complex fluctuations in the window position as well as shell structure, those quantities show rapid fluctuations as a function of time. In order to eliminate the rapid fluctuations in time, we carry out a smoothing by taking an average over a short time interval,  $T_{\text{ave}} \simeq 0.67$  zs. In Fig. A1, we show the smoothed mean neutron and proton numbers in the projectile-like subsystem,  $N_1(t)$  (red solid line) and  $Z_1(t)$  (green dashed line), in the  $^{64}\text{Ni}+^{208}\text{Pb}$  reaction at  $E_{\text{c.m.}} = 268$  MeV with the initial orbital angular momentum  $L = 50\hbar$  as a function of time. One can see that there is a fast charge equilibration process (from  $t_A$  to  $t_B$ ), followed by a slow mass equilibration process (from  $t_B$  to  $t_C$ ), during the collision process.

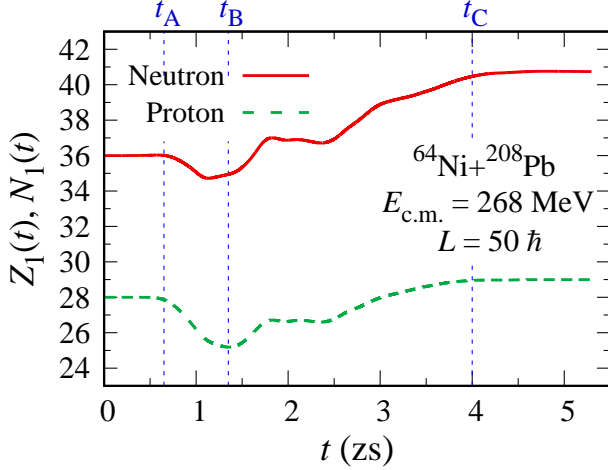


FIG. A1. The smoothed mean values of the neutron and proton numbers of the projectile-like subsystem in the  $^{64}\text{Ni}+^{208}\text{Pb}$  reaction at  $E_{c.m.} = 268$  MeV with the initial orbital angular momentum  $L = 50\hbar$  as a function of time. Red solid line shows that of neutrons,  $N_1(t)$ , while the green dashed line shows that of protons,  $Z_1(t)$ .

In Fig. A2, the same quantities as shown in Fig. A1 are shown, but now they are plotted in the  $N$ - $Z$  plane, which we call the drift path. In the figure, green dashed line indicates a collection of nuclei with nearly same charge asymmetry values,  $\delta = (N - Z)/(N + Z) = 0.16\text{--}0.19$ . We call this line the isoscalar path which extends along the beta-stability valley until the mass equilibrium at  $N_0 = (36 + 126)/2 = 81$  and  $Z_0 = (28 + 82)/2 = 55$ . Starting from the point A, the  $(N_1, Z_1)$  follows the red solid line until it reaches the charge equilibrium at  $\delta \simeq 0.16$  at the point B and drifts toward the mass symmetry nearly along the isoscalar path. Note that the binary system separates before reaching the mass equilibrium of the system.

The potential energy surface of the dinuclear system with respect to  $(N_1, Z_1)$  provided by the microscopic Skyrme energy density functional would have a rather complex structure. Here, we approximate the potential by a two-parabolic form: One parabola is along the isoscalar direction and the other is perpendicular to it, which we call the isovector path. Namely, the driving potential is expressed as

$$U(N_1, Z_1) = \frac{1}{2}aR_S^2 + \frac{1}{2}bR_E^2, \quad (\text{A1})$$

where

$$R_S = [N_0 - N_1] \sin \phi - [Z_0 - Z_1] \cos \phi, \quad (\text{A2})$$

$$R_E = [N_0 - N_1] \cos \phi + [Z_0 - Z_1] \sin \phi. \quad (\text{A3})$$

$R_S(t)$  represents the distance of  $(N_1, Z_1)$  on the drift path from the isoscalar path, while  $R_E(t)$  represents the distance of  $(N_1, Z_1)$  from the equilibrium point  $(N_0, Z_0)$  along the isoscalar path. The angle,  $\phi = 32.9^\circ$ , denotes the angle between the isoscalar path and the neutron axis. The Einstein relation relates the drift coefficients to the derivatives of the

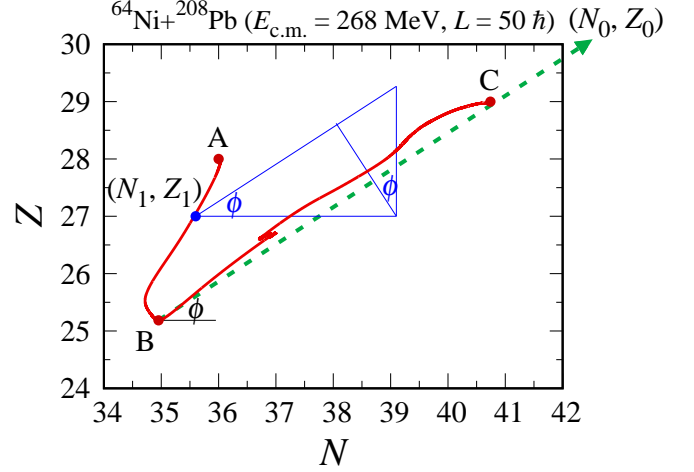


FIG. A2. The smoothed mean drift path in the  $N$ - $Z$  plane for the projectile-like subsystem in the  $^{64}\text{Ni}+^{208}\text{Pb}$  reaction at  $E_{c.m.} = 268$  MeV with the initial orbital angular momentum  $L = 50\hbar$ . Green dashed arrow indicates the isoscalar path which continues along the mass symmetry point,  $(N_0, Z_0) = (81, 55)$ . The angle  $\phi = 32.9^\circ$  is the angle between the isoscalar path and the neutron axis. The points A, B, and C correspond to the time  $t_A$ ,  $t_B$ , and  $t_C$  in Fig. A1, respectively. Blue triangles help to understand the distances, Eqs. (A2) and (A3).

potential energy surface according to

$$\nu_n = -\frac{D_{NN}}{T^*} \frac{\partial}{\partial N_1} U(N_1, Z_1), \quad (\text{A4})$$

$$\nu_p = -\frac{D_{ZZ}}{T^*} \frac{\partial}{\partial Z_1} U(N_1, Z_1). \quad (\text{A5})$$

Using the two-parabolic form of the potential (A1), one finds analytical expressions of the drift coefficients:

$$\nu_n(t) = +D_{NN}(t) [\alpha R_S(t) \sin \phi + \beta R_E(t) \cos \phi], \quad (\text{A6})$$

$$\nu_p(t) = -D_{ZZ}(t) [\alpha R_S(t) \cos \phi - \beta R_E(t) \sin \phi]. \quad (\text{A7})$$

Note that the effective temperature  $T^*$  has been absorbed to the curvature parameters,  $\alpha = a/T^*$  and  $\beta = b/T^*$ . Having those analytical forms at hand, one can readily calculate the derivatives of the drift coefficients, i.e.,

$$\frac{\partial \nu_n(t)}{\partial N_1} = -D_{NN}(t) [\alpha \sin^2 \phi + \beta \cos^2 \phi], \quad (\text{A8})$$

$$\frac{\partial \nu_p(t)}{\partial Z_1} = -D_{ZZ}(t) [\alpha \cos^2 \phi + \beta \sin^2 \phi], \quad (\text{A9})$$

$$\frac{\partial \nu_n(t)}{\partial Z_1} = D_{NN}(t) (\alpha - \beta) \sin \phi \cos \phi, \quad (\text{A10})$$

$$\frac{\partial \nu_p(t)}{\partial N_1} = D_{ZZ}(t) (\alpha - \beta) \sin \phi \cos \phi. \quad (\text{A11})$$

The remaining task is to determine the reduced curvature parameters,  $\alpha$  and  $\beta$ . Actually, the latter quantities can be determined with the mean drift coefficients,  $\nu_n(t) = dN_1(t)/dt$  and  $\nu_p(t) = dZ_1(t)/dt$ , obtained from TDHF. From Eqs. (A6)

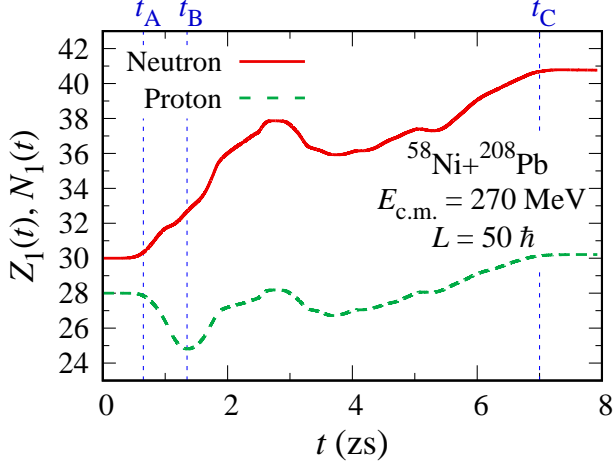


FIG. A3. Same as Fig. A1, but for the  $^{58}\text{Ni}+^{208}\text{Pb}$  reaction at  $E_{\text{c.m.}} = 270$  MeV with the initial orbital angular momentum  $L = 50\hbar$ .

and (A7), we have the following equalities:

$$\alpha R_S(t) = \frac{\nu_n(t) \sin \phi}{D_{NN}(t)} - \frac{\nu_p(t) \cos \phi}{D_{ZZ}(t)}, \quad (\text{A12})$$

$$\beta R_E(t) = \frac{\nu_n(t) \cos \phi}{D_{NN}(t)} + \frac{\nu_p(t) \sin \phi}{D_{ZZ}(t)}. \quad (\text{A13})$$

To derive macroscopic drift coefficients for the nucleon diffusion mechanism, we need to eliminate microscopic effects on the potential energy, e.g., complex dynamic shell effects. Namely, due to the complex structure of the microscopic potential energy surface in TDHF, the reduced curvature parameters of the simple parabolic approximation may vary in time. We thus take the following time average to determine the average reduced curvature parameters:

$$\bar{\alpha} = \int_{t_A}^{t_B} \left( \frac{\nu_n(t) \sin \phi}{D_{NN}(t)} - \frac{\nu_p(t) \cos \phi}{D_{ZZ}(t)} \right) dt \Big/ \int_{t_A}^{t_B} R_S(t) dt, \quad (\text{A14})$$

$$\bar{\beta} = \int_{t_B}^{t_C} \left( \frac{\nu_n(t) \cos \phi}{D_{NN}(t)} + \frac{\nu_p(t) \sin \phi}{D_{ZZ}(t)} \right) dt \Big/ \int_{t_B}^{t_C} R_E(t) dt. \quad (\text{A15})$$

Note that all quantities in the right-hand side of Eqs. (A14) and (A15) can be computed within the TDHF approach. Here,  $t_A = 0.65$  zs,  $t_B = 1.35$  zs, and  $t_C = 4.00$  zs indicate the times at the points A, B, and C, respectively, in Figs. A1 and A2. For the  $^{64}\text{Ni}+^{208}\text{Pb}$  system, we obtained the average reduced curvature parameters of  $\bar{\alpha} = 0.289$  and  $\bar{\beta} = 0.003$  for the isovector and isoscalar directions, respectively. With those  $\bar{\alpha}$  and  $\bar{\beta}$ , the derivatives of the drift coefficients, Eqs. (A8)–(A11), were evaluated.

## 2. For the $^{58}\text{Ni}+^{208}\text{Pb}$ system

Figures A3 and A4 show the time evolution of the smoothed mean neutron and proton numbers in the projectile-like subsystem in the  $^{58}\text{Ni}+^{208}\text{Pb}$  reaction at  $E_{\text{c.m.}} = 270$  MeV with the initial orbital angular momentum  $L = 50\hbar$ .

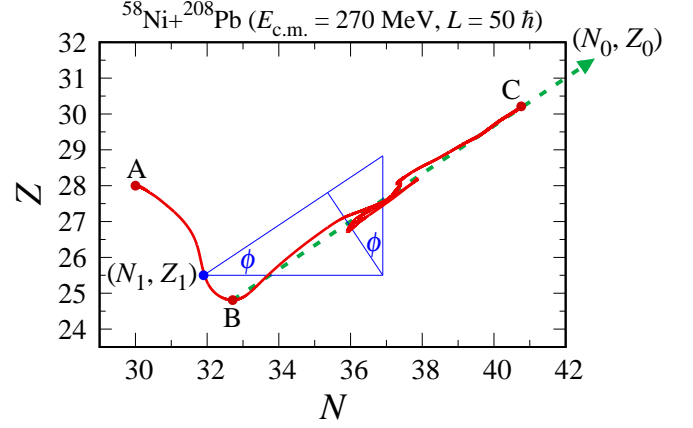


FIG. A4. Same as Fig. A2, but for the  $^{58}\text{Ni}+^{208}\text{Pb}$  reaction at  $E_{\text{c.m.}} = 270$  MeV with the initial orbital angular momentum  $L = 50\hbar$ . The mass symmetry point is  $(N_0, Z_0) = (78, 55)$  and the angle between the isoscalar path and the neutron axis is  $\phi = 33.3^\circ$ .

Basically, we repeat the same procedure also for the  $^{58}\text{Ni}+^{208}\text{Pb}$  system. The times  $t_A = 0.65$  zs,  $t_B = 1.35$  zs, and  $t_C = 7.00$  zs of the averaging intervals indicated in Fig. A3 correspond to the points A, B, and C in Fig. A4, respectively. In the isoscalar drift path of this system between the points B and C in Fig. A4, the nuclei have nearly the same charge asymmetry values of  $\delta = 0.14\text{--}0.17$ . The angle between the isoscalar path and the neutron axis is  $\phi = 33.3^\circ$ , which is similar to the one for the  $^{64}\text{Ni}+^{208}\text{Pb}$  system. The equilibrium values of neutron and proton numbers are  $N_0 = (30 + 126)/2 = 78$  and  $Z_0 = (28 + 82)/2 = 55$ . The average curvature parameters evaluated by Eqs. (A14) and (A15) have nearly the same magnitude as those for the  $^{64}\text{Ni}+^{208}\text{Pb}$  system, which are given by  $\bar{\alpha} = 0.247$  and  $\bar{\beta} = 0.002$  for the isovector and isoscalar directions, respectively.

We note that the isoscalar line (green dashed arrow) in Figs. A2 and A4 should be extended further until the mass equilibrium point,  $(N_0, Z_0)$ .

## Appendix B: Tables of the TDHF and SMF results

Here, we provide the numerical results of the TDHF and SMF calculations for the  $^{64}\text{Ni}+^{208}\text{Pb}$  reaction at  $E_{\text{c.m.}} = 268$  MeV in Table I and for the  $^{58}\text{Ni}+^{208}\text{Pb}$  reaction at  $E_{\text{c.m.}} = 270$  MeV in Table II with various initial conditions.

TABLE I. Results of the TDHF and SMF calculations for the  $^{64}\text{Ni}+^{208}\text{Pb}$  reaction at  $E_{\text{c.m.}} = 268$  MeV. From left to right columns, the table lists: the initial orbital angular momentum  $L_i$  in  $\hbar$ , the corresponding impact parameter  $b$  in fm, the final values of the average proton and neutron numbers in a projectile-like fragment (PLF) ( $Z_1^f$  and  $N_1^f$ ) and a target-like fragment (TLF) ( $Z_2^f$  and  $N_2^f$ ), the final orbital angular momentum  $L_f$  in  $\hbar$ , the total kinetic energy loss (TKEL) in MeV, the contact time  $t_{\text{contact}}$  in zeptoseconds ( $1 \text{ zs} = 10^{-21} \text{ s}$ ), the dispersions by SMF ( $\sigma_{NN}$ ,  $\sigma_{ZZ}$ ,  $\sigma_{NZ}$ , and  $\sigma_{AA}$ ) and the mass dispersion by TDHF ( $\sigma_{AA}$ ), and the scattering angles in the center-of-mass frame ( $\theta_{\text{c.m.}}$ ) and in the laboratory frame for a PLF ( $\vartheta_1^{\text{lab}}$ ) and a TLF ( $\vartheta_2^{\text{lab}}$ ) in degrees.

$L_i$ ( $\hbar$ )	$b$ (fm)	$Z_1^f$	$N_1^f$	$Z_2^f$	$N_2^f$	$L_f$ ( $\hbar$ )	TKEL (MeV)	$t_{\text{contact}}$ (zs)	$\sigma_{NN}$	$\sigma_{ZZ}$	$\sigma_{NZ}$	$\sigma_{AA}$	$\sigma_{AA}^{\text{TDHF}}$	$\theta_{\text{c.m.}}$	$\vartheta_1^{\text{lab}}$	$\vartheta_2^{\text{lab}}$ (deg)
0	0.00	27.75	37.99	82.23	123.81	0.0	64.1	4.66	11.98	7.85	9.50	19.64	1.94	180.0	180.0	0.0
5	0.20	27.73	37.98	82.24	123.83	4.3	64.3	4.62	11.92	7.81	9.45	19.53	1.94	169.9	164.3	4.7
10	0.40	27.69	37.95	82.29	123.85	8.4	65.2	4.56	11.85	7.77	9.40	19.43	1.94	160.2	149.8	9.3
15	0.60	27.60	37.88	82.37	123.91	12.8	66.9	4.45	11.80	7.74	9.36	19.34	1.94	150.8	136.4	13.7
20	0.80	27.49	37.79	82.48	123.99	17.4	68.7	4.36	11.74	7.70	9.30	19.24	1.94	141.8	124.4	17.8
25	0.99	27.48	37.87	82.49	123.92	21.0	70.7	4.37	11.30	7.41	8.94	18.50	1.94	133.2	113.8	21.7
30	1.19	27.72	38.25	82.26	123.55	23.5	71.5	4.35	11.24	7.37	8.89	18.41	1.96	125.4	104.7	25.3
35	1.39	28.14	38.83	81.83	122.99	25.1	70.0	4.30	11.16	7.32	8.83	18.27	1.97	118.5	97.1	28.7
40	1.59	28.40	39.34	81.57	122.50	27.1	67.9	4.10	11.01	7.23	8.71	18.03	1.97	112.4	90.7	31.7
45	1.79	28.62	39.86	81.36	121.99	33.3	65.0	3.82	10.76	7.06	8.50	17.61	1.98	106.7	85.1	34.6
50	1.99	28.99	40.69	80.99	121.18	37.3	62.3	3.57	10.41	6.83	8.20	17.02	1.91	104.4	82.8	36.1
55	2.19	29.31	41.14	80.67	120.73	41.6	61.8	3.23	10.00	6.56	7.86	16.33	1.91	102.8	81.1	37.1
60	2.39	29.33	41.09	80.66	120.77	46.0	65.1	3.02	9.67	6.36	7.60	15.79	1.92	99.8	78.1	38.3
65	2.59	29.27	40.94	80.72	120.93	49.6	66.3	2.82	9.34	6.13	7.31	15.23	1.94	96.7	75.3	39.6
70	2.79	29.19	40.86	80.80	121.03	53.8	64.1	2.54	8.95	5.88	6.99	14.58	1.91	94.2	73.2	40.9
75	2.98	29.12	40.99	80.87	120.91	59.2	63.1	2.34	8.56	5.63	6.66	13.92	1.88	91.8	71.1	42.1
80	3.18	29.26	41.15	80.73	120.76	63.9	62.6	2.15	8.16	5.37	6.33	13.25	1.86	90.5	69.9	42.8
85	3.38	29.29	40.73	80.70	121.18	67.5	62.3	1.96	7.74	5.10	5.98	12.55	1.85	90.0	69.6	42.9
90	3.58	28.96	39.90	81.04	122.03	70.7	62.3	1.79	7.31	4.83	5.61	11.82	1.85	89.8	69.6	42.7
95	3.78	28.61	39.05	81.38	122.86	76.9	65.7	1.69	6.85	4.53	5.22	11.04	1.85	88.6	68.6	42.7
100	3.98	27.89	37.84	82.10	124.07	80.8	70.0	1.48	6.28	4.18	4.74	10.09	1.80	88.5	68.7	41.8
110	4.38	26.92	36.81	83.06	125.10	86.9	66.9	1.02	5.16	3.45	3.74	8.16	1.68	91.4	71.7	40.2
120	4.77	26.77	36.69	83.22	125.23	100.1	54.0	0.66	4.12	2.79	2.78	6.34	1.50	92.8	73.6	40.4
130	5.17	27.30	36.45	82.70	125.52	118.5	29.9	0.02	2.85	1.79	1.38	3.89	1.16	93.5	75.1	41.6
140	5.57	27.86	36.20	82.14	125.80	137.0	6.1	0.00	1.72	0.92	0.41	2.03	0.74	93.2	75.7	43.1
150	5.97	27.96	36.10	82.04	125.90	148.8	2.3	0.00	1.20	0.64	0.20	1.39	0.52	90.5	73.3	44.6
160	6.37	27.98	36.06	82.02	125.94	159.4	1.3	0.00	0.92	0.50	0.12	1.06	0.40	87.4	70.5	46.3
170	6.76	27.99	36.03	82.01	125.96	169.7	0.9	0.00	0.73	0.40	0.08	0.84	0.32	84.2	67.6	47.9
180	7.16	28.00	36.02	82.00	125.98	179.9	0.7	0.00	0.60	0.33	0.05	0.69	0.26	81.1	64.9	49.4
190	7.56	28.00	36.01	82.00	125.98	189.9	0.5	0.00	0.50	0.27	0.03	0.57	0.21	78.2	62.3	50.9
200	7.96	28.00	36.01	82.00	125.99	200.0	0.4	0.00	0.42	0.22	0.02	0.48	0.17	75.4	59.9	52.3
210	8.36	28.00	36.01	82.00	125.99	210.0	0.4	0.00	0.36	0.18	0.02	0.40	0.13	72.7	57.7	53.6
220	8.75	28.00	36.00	82.00	126.00	220.0	0.3	0.00	0.31	0.15	0.01	0.34	0.11	70.2	55.5	54.9
230	9.15	28.00	36.00	82.00	126.00	230.0	0.3	0.00	0.26	0.12	0.01	0.29	0.09	67.9	53.6	56.0
240	9.55	28.00	36.00	82.00	126.00	240.0	0.3	0.00	0.23	0.10	0.01	0.25	0.07	65.7	51.7	57.1

TABLE II. Same as Table I, but for the  $^{58}\text{Ni}+^{208}\text{Pb}$  reaction at  $E_{\text{c.m.}} = 270$  MeV.

$L_i$ ( $\hbar$ )	$b$ (fm)	$Z_1^f$	$N_1^f$	$Z_2^f$	$N_2^f$	$L_f$ ( $\hbar$ )	TKEL (MeV)	$t_{\text{contact}}$ (zs)	$\sigma_{NN}$	$\sigma_{ZZ}$	$\sigma_{NZ}$	$\sigma_{AA}$	$\sigma_{AA}^{\text{TDHF}}$	$\theta_{\text{c.m.}}$	$\vartheta_1^{\text{lab}}$	$\vartheta_2^{\text{lab}}$ (deg)
50	2.06	30.20	40.70	79.77	115.12	36.7	67.8	6.21	13.42	9.04	10.81	22.26	2.10	57.8	43.2	60.5
55	2.26	29.78	39.57	80.20	116.32	40.6	61.4	4.38	11.63	7.84	9.31	19.24	2.03	77.0	59.1	51.1
60	2.47	29.37	39.07	80.61	116.84	43.4	62.0	3.11	9.75	6.58	7.73	16.06	2.00	92.1	72.4	43.3
65	2.68	29.28	39.18	80.70	116.74	50.1	64.1	2.71	8.98	6.07	7.08	14.76	1.98	91.8	72.0	43.4
70	2.88	28.73	37.99	81.25	117.92	53.6	71.7	2.36	8.35	5.65	6.54	13.68	2.07	90.8	71.1	42.8
75	3.09	28.44	36.85	81.54	119.08	60.3	70.9	2.01	7.52	5.10	5.83	12.27	2.04	92.6	73.0	41.6
80	3.29	27.32	35.17	82.66	120.74	58.8	75.3	1.57	6.52	4.44	4.96	10.56	1.97	97.6	77.9	38.3
85	3.50	26.42	34.04	83.56	121.87	63.6	73.9	1.19	5.57	3.82	4.11	8.92	1.82	99.9	80.5	36.9
90	3.71	25.78	33.17	84.20	122.74	73.1	70.7	0.70	4.85	3.33	3.43	7.63	1.76	99.9	81.0	36.7
95	3.91	26.00	33.16	83.99	122.77	80.2	59.1	0.49	4.21	2.90	2.80	6.47	1.66	101.1	82.6	36.9
100	4.12	26.21	32.73	83.79	123.22	88.9	44.1	0.29	3.54	2.42	2.10	5.21	1.46	101.9	84.0	37.2
110	4.53	27.48	31.80	82.52	124.19	106.0	12.6	0.00	2.24	1.32	0.74	2.81	1.10	102.3	85.6	38.6
120	4.94	27.84	30.93	82.16	125.07	117.8	4.1	0.00	1.58	0.85	0.33	1.86	0.88	99.9	83.6	40.1
130	5.35	27.93	30.56	82.07	125.44	128.3	2.4	0.00	1.23	0.66	0.20	1.43	0.72	96.2	80.1	41.9
140	5.76	27.96	30.35	82.04	125.65	138.6	1.8	0.00	0.99	0.54	0.13	1.14	0.58	92.4	76.6	43.8
150	6.18	27.98	30.23	82.02	125.77	148.8	1.4	0.00	0.80	0.45	0.09	0.93	0.48	88.7	73.2	45.6
160	6.59	27.99	30.15	82.01	125.85	159.0	1.2	0.00	0.65	0.38	0.06	0.76	0.39	85.2	69.9	47.4
170	7.00	27.99	30.09	82.01	125.90	169.1	1.0	0.00	0.53	0.32	0.04	0.63	0.31	81.8	66.9	49.1
180	7.41	28.00	30.06	82.00	125.94	179.2	0.9	0.00	0.44	0.27	0.03	0.52	0.25	78.7	64.1	50.6
190	7.82	28.00	30.04	82.00	125.96	189.3	0.8	0.00	0.36	0.23	0.02	0.43	0.20	75.7	61.5	52.1
200	8.23	28.00	30.02	82.00	125.97	199.3	0.7	0.00	0.30	0.19	0.01	0.36	0.16	72.9	59.1	53.5
210	8.65	28.00	30.02	82.00	125.98	209.4	0.7	0.00	0.25	0.16	0.01	0.30	0.13	70.3	56.8	54.8
220	9.06	28.00	30.01	82.00	125.99	219.4	0.6	0.00	0.21	0.14	0.01	0.25	0.10	67.8	54.7	56.0
230	9.47	28.00	30.01	82.00	125.99	229.5	0.6	0.00	0.17	0.12	0.00	0.21	0.08	65.5	52.7	57.2
240	9.88	28.00	30.00	82.00	126.00	239.5	0.5	0.00	0.15	0.10	0.00	0.18	0.07	63.3	50.8	58.3

- [1] M. Thoennessen, Discovery of nuclides project, <https://people.nsl.msui.edu/~thoenness/isotopes/>.
- [2] V. Zagrebaev and W. Greiner, Production of New Heavy Isotopes in Low-Energy Multinucleon Transfer Reactions, *Phys. Rev. Lett.* **101**, 122701 (2008).
- [3] T. Otsuka, A. Gade, O. Sorlin, T. Suzuki, and Y. Utsuno, Evolution of shell structure in exotic nuclei, *Rev. Mod. Phys.* **92**, 015002 (2020).
- [4] S. Hofmann and G. Münzenberg, The discovery of the heaviest elements, *Rev. Mod. Phys.* **72**, 733 (2000).
- [5] Yu. Ts. Oganessian, A. Sobiczewski, and G.M. Ter-Akopian, Superheavy nuclei: from predictions to discovery, *Phys. Scr.* **92**, 023003 (2017).
- [6] T. Kajino, W. Aoki, A.B. Balantekin, R. Diehl, M.A. Famiano, G.J. Mathews, Current status of r-process nucleosynthesis, *Prog. Part. Nucl. Phys.* **107**, 109 (2019).
- [7] G.G. Adamian, N.V. Antonenko, A. Diaz-Torres, and S. Heinz, How to extend the chart of nuclides?, *Eur. Phys. J. A* **56**, 47 (2020).
- [8] A. Winther, Grazing reactions in collisions between heavy nuclei, *Nucl. Phys.* **A572**, 191 (1994).
- [9] A. Winther, Dissipation, polarization and fluctuation in grazing heavy-ion collisions and the boundary to the chaotic regime, *Nucl. Phys.* **A594**, 203 (1995).
- [10] E. Vigezzi and A. Winther, On the Application of Complex Trajectories to Direct Heavy-Ion Reactions, *Ann. Phys. (N.Y.)* **192**, 432 (1989).
- [11] R. Yanez and W. Loveland, Predicting the production of neutron-rich heavy nuclei in multinucleon transfer reactions using a semi-classical model including evaporation and fission competition, *GRAZING-F*, *Phys. Rev. C* **91**, 044608 (2015).
- [12] P.W. Wen, C.J. Lin, C. Li, L. Zhu, F. Zhang, F.S. Zhang, H.M. Jia, F. Yang, N.R. Ma, L.J. Sun, D.X. Wang, F.P. Zhong, H.H. Sun, L. Yang, and X.X. Xu, Evaporation and fission of the primary fragments produced by multinucleon transfer reactions, *Phys. Rev. C* **99**, 034606 (2019).
- [13] L. Zhu, Theoretical study on production of exotic nuclei near the neutron-drip line in multinucleon transfer reactions, *J. Phys. G: Nucl. Part. Phys.* **46**, 065102 (2019).
- [14] G. Zhang, C.A.T. Sokhna, Z. Liu, and F.-S. Zhang, Production of neutron-rich isotopes  $^{264,266,268,269}\text{Rf}$  by multinucleon transfer reactions based on  $^{238}\text{U}$  beam, *Phys. Rev. C* **100**, 024613 (2019).
- [15] S.Q. Guo, X.J. Bao, H.F. Zhang, J.Q. Li, and N. Wang, Effect of dynamical deformation on the production distribution in multinucleon transfer reactions, *Phys. Rev. C* **100**, 054616 (2019).
- [16] P.-H. Chen, F. Niu, W. Zuo, and Z.-Q. Feng, Approaching the neutron-rich heavy and superheavy nuclei by multinucleon transfer reactions with radioactive isotopes, *Phys. Rev. C* **101**, 024610 (2020).
- [17] Yu.E. Penionzhkevich, G.G. Adamian, and N.V. Antonenko, Towards neutron drip line via transfer-type reactions, *Phys. Lett.* **B621**, 119 (2005).
- [18] Yu.E. Penionzhkevich, G.G. Adamian, and N.V. Antonenko, Production of neutron-rich Ca isotopes in transfer-type reactions, *Eur. Phys. J. A* **27**, 187 (2006).
- [19] M.-H. Mun, G.G. Adamian, N.V. Antonenko, Y. Oh, and Y. Kim, Production cross section of neutron-rich isotopes with radioactive and stable beams, *Phys. Rev. C* **89**, 034622 (2014).
- [20] M.-H. Mun, G.G. Adamian, N.V. Antonenko, Y. Oh, and Y. Kim, Toward neutron-rich nuclei via transfer reactions with stable and radioactive beams, *Phys. Rev. C* **91**, 054610 (2015).
- [21] M.-H. Mun, K. Kwak, G.G. Adamian, and N.V. Antonenko, Possible production of neutron-rich Md isotopes in multinucleon transfer reactions with Cf and Es targets, *Phys. Rev. C* **99**, 054627 (2019).
- [22] T. Welsh, W. Loveland, R. Yanez, J.S. Barrett, E.A. McCutchan, A.A. Sonzogni, T. Johnson, S. Zhu, J.P. Greene, A.D. Ayangeakaa, M.P. Carpenter, T. Lauritsen, J.L. Harker, W.B. Walters, B.M.S. Amro, and P. Copp, Modeling multi-nucleon transfer in symmetric collisions of massive nuclei, *Phys. Lett.* **B771**, 119 (2017).
- [23] P.-W. Wen, C. Li, L. Zhu, C.-J. Lin, and F.-S. Zhang, Mechanism of multinucleon transfer reaction based on the GRAZING model and DNS model, *J. Phys. G: Nucl. Part. Phys.* **44**, 115101 (2017).
- [24] V. Zagrebaev and W. Greiner, Shell effects in damped collisions: a new way to superheavies, *J. Phys. G: Nucl. Part. Phys.* **34**, 2265 (2007).
- [25] V. Zagrebaev and W. Greiner, Low-energy collisions of heavy nuclei: dynamics of sticking, mass transfer and fusion, *J. Phys. G: Nucl. Part. Phys.* **34**, 1 (2007).
- [26] A.V. Karpov and V.V. Saiko, Modeling near-barrier collisions of heavy ions based on a Langevin-type approach, *Phys. Rev. C* **96**, 024618 (2017).
- [27] V. Saiko and A. Karpov, Analysis of multinucleon transfer reactions involving spherical and statically deformed nuclei using a Langevin-type approach, *Phys. Rev. C* **99**, 014613 (2019).
- [28] N. Wang and Lu Guo, New neutron-rich isotope production in  $^{154}\text{Sm}+^{160}\text{Gd}$ , *Phys. Lett.* **B760**, 236 (2016).
- [29] C. Li, F. Zhang, J. Li, L. Zhu, J. Tian, N. Wang, and F.-S. Zhang, Multinucleon transfer in the  $^{136}\text{Xe}+^{208}\text{Pb}$  reaction, *Phys. Rev. C* **93**, 014618 (2016).
- [30] K. Zhao, Z. Li, Y. Zhang, N. Wang, Q. Li, C. Shen, Y. Wang, and X. Wu, Production of unknown neutron-rich isotopes in  $^{238}\text{U}+^{238}\text{U}$  collisions at near-barrier energy, *Phys. Rev. C* **94**, 024601 (2016).
- [31] C. Li, X. Xu, J. Li, G. Zhang, B. Li, C.A.T. Sokhna, Z. Ge, F. Zhang, P. Wen, and F.-S. Zhang, Production of new neutron-rich heavy nuclei with  $Z = 56-80$  in the multinucleon transfer reactions of  $^{136}\text{Xe}+^{198}\text{Pt}$ , *Phys. Rev. C* **99**, 024602 (2019).
- [32] L. Corradi, G. Pollarolo, and S. Szilner, Multinucleon transfer processes in heavy-ion reactions, *J. Phys. G: Nucl. Part. Phys.* **36**, 113101 (2009).
- [33] F.-S. Zhang, C. Li, L. Zhu, and P. Wen, Production cross sections for exotic nuclei with multinucleon transfer reactions *Front. Phys.* **13**, 132113 (2018).
- [34] K. Sekizawa, TDHF Theory and Its Extensions for Multinucleon Transfer Reactions: A Mini Review, *Front. Phys.* **7**, 20 (2019).
- [35] R. Balian and M. Vénéroni, Time-Dependent Variational Principle for Predicting the Expectation Value of an Observable, *Phys. Rev. Lett.* **47**, 1353 (1981); **47**, 1765 (1981).
- [36] C. Simenel, Nuclear quantum many-body dynamics, *Eur. Phys. J. A* **48**, 152 (2012).
- [37] C. Simenel, Particle Transfer Reactions with the Time-Dependent Hartree-Fock Theory Using a Particle Number Projection Technique, *Phys. Rev. Lett.* **105**, 192701 (2010).

- [38] K. Sekizawa and K. Yabana, Time-dependent Hartree-Fock calculations for multinucleon transfer processes in  $^{40,48}\text{Ca}+^{124}\text{Sn}$ ,  $^{40}\text{Ca}+^{208}\text{Pb}$ , and  $^{58}\text{Ni}+^{208}\text{Pb}$  reactions, Phys. Rev. C **88**, 014614 (2013); **93**, 029902(E) (2016).
- [39] K. Sekizawa, Microscopic description of production cross sections including deexcitation effects, Phys. Rev. C **96**, 014615 (2017).
- [40] K. Sekizawa and K. Yabana, Particle-number projection method in time-dependent Hartree-Fock theory, Phys. Rev. C **90**, 064614 (2014).
- [41] Sonika, B.J. Roy, A. Parmar, U.K. Pal, H. Kumawat, V. Jha, S.K. Pandit, V.V. Parkar, K. Ramachandran, K. Mahata, A. Pal, S. Santra, A.K. Mohanty, and K. Sekizawa, Multinucleon transfer study in  $^{206}\text{Pb}(^{18}\text{O}, x)$  at energies above the Coulomb barrier, Phys. Rev. C **92**, 024603 (2015).
- [42] K. Sekizawa and K. Yabana, Time-dependent Hartree-Fock calculations for multinucleon transfer and quasifission processes in the  $^{64}\text{Ni}+^{238}\text{U}$  reaction, Phys. Rev. C **93**, 054616 (2016).
- [43] K. Sekizawa, Enhanced nucleon transfer in tip collisions of  $^{238}\text{U}+^{124}\text{Sn}$ , Phys. Rev. C **96**, 041601(R) (2017).
- [44] B.J. Roy, Y. Sawant, P. Patwari, S. Santra, A. Pal, A. Kundu, D. Chattopadhyay, V. Jha, S.K. Pandit, V.V. Parkar, K. Ramachandran, K. Mahata, B.K. Nayak, A. Saxena, S. Kailas, T.N. Nag, R.N. Sahoo, P.P. Singh, and K. Sekizawa, Deep-inelastic multinucleon transfer processes in the  $^{16}\text{O}+^{27}\text{Al}$  reaction, Phys. Rev. C **97**, 034603 (2018).
- [45] Z. Wu and Lu Guo, Microscopic studies of production cross sections in multinucleon transfer reaction  $^{58}\text{Ni}+^{124}\text{Sn}$  Phys. Rev. C **100**, 014612 (2019).
- [46] X. Jiang and N. Wang, Production mechanism of neutron-rich nuclei around  $N = 126$  in the multinucleon transfer reaction  $^{132}\text{Sn}+^{208}\text{Pb}$ , Chin. Phys. C **42**, 104105 (2018).
- [47] X. Jiang and N. Wang, Probing the production mechanism of neutron-rich nuclei in multinucleon transfer reactions, Phys. Rev. C **101**, 014604 (2020).
- [48] X. Jiang and N. Wang, Predictions of New Neutron-Rich Isotopes at  $N = 126$  in the Multinucleon Transfer Reaction  $^{136}\text{Xe}+^{194}\text{Ir}$ , Front. Phys. **8**, 38 (2020).
- [49] A.S. Umar, C. Simenel, and W. Ye, Transport properties of isospin asymmetric nuclear matter using the time-dependent Hartree-Fock method, Phys. Rev. C **96**, 024625 (2017).
- [50] L. Guo, C. Shen, C. Yu, and Z. Wu, Isotopic trends of quasifission and fusion-fission in the reactions  $^{48}\text{Ca}+^{239,244}\text{Pu}$ , Phys. Rev. C **98**, 064609 (2018).
- [51] S.E. Koonin, K.T.R. Davies, V. Maruhn-Rezwani, H. Feldmeier, S.J. Krieger, and J.W. Negele, Time-dependent Hartree-Fock calculations for  $^{16}\text{O}+^{16}\text{O}$  and  $^{40}\text{Ca}+^{40}\text{Ca}$  reactions, Phys. Rev. C **15**, 1359 (1977).
- [52] C.H. Dasso, T. Døssing, and H.C. Pauli, On the mass distribution in Time-Dependent Hartree-Fock calculations of heavy-ion collisions, Z. Phys. A **289**, 395 (1979).
- [53] J.M.A. Broomfield and P.D. Stevenson, Mass distributions beyond TDHF, in *FUSION08: New Aspects of Heavy Ion Collisions Near the Coulomb Barrier*, edited by K.E. Rehm, B.B. Back, H. Esbensen, and C.J. (Kim) Lister, AIP Conf. Proc. No. 1098 (AIP, New York, 2009), p. 133.
- [54] C. Simenel, Particle-Number Fluctuations and Correlations in Transfer Reactions Obtained Using the Balian-Vénéroni Variational Principle, Phys. Rev. Lett. **106**, 112502 (2011).
- [55] E. Williams, K. Sekizawa, D.J. Hinde, C. Simenel, M. Dasgupta, I.P. Carter, K.J. Cook, D.Y. Jeung, S.D. McNeil, C.S. Palshetkar, D.C. Rafferty, K. Ramachandran, and A. Wakhle, Exploring Zeptosecond Quantum Equilibration Dynamics: From Deep-Inelastic to Fusion-Fission Outcomes in  $^{58}\text{Ni}+^{60}\text{Ni}$  Reactions, Phys. Rev. Lett. **120**, 022501 (2018).
- [56] K. Godbey, C. Simenel, and A.S. Umar, Microscopic predictions for production of neutron rich nuclei in the reaction  $^{176}\text{Yb}+^{176}\text{Yb}$ , Phys. Rev. C **101**, 034602 (2020).
- [57] S. Ayik, A stochastic mean-field approach for nuclear dynamics, Phys. Lett. **B658**, 174 (2008).
- [58] E. Nelson, Derivation of the Schrödinger Equation from Newtonian Mechanics, Phys. Rev. **150**, 1079 (1966).
- [59] D. Lacroix, Y. Tanimura, S. Ayik, and B. Yilmaz, A simplified BBGKY hierarchy for correlated fermions from a stochastic mean-field approach, Eur. Phys. J. A **52**, 94 (2016).
- [60] D. Lacroix and S. Ayik, Stochastic quantum dynamics beyond mean field, Eur. Phys. J. A **50**, 95 (2014).
- [61] S. Ayik, K. Washiyama, and D. Lacroix, Fluctuation and dissipation dynamics in fusion reactions from a stochastic mean-field approach, Phys. Rev. C **79**, 054606 (2009).
- [62] K. Washiyama, S. Ayik, and D. Lacroix, Mass dispersion in transfer reactions with a stochastic mean-field theory, Phys. Rev. C **80**, 031602(R) (2009).
- [63] B. Yilmaz, S. Ayik, D. Lacroix, and K. Washiyama, Nucleon exchange mechanism in heavy-ion collisions at near-barrier energies, Phys. Rev. C **83**, 064615 (2011).
- [64] B. Yilmaz, S. Ayik, D. Lacroix, and O. Yilmaz, Nucleon exchange in heavy-ion collisions within a stochastic mean-field approach, Phys. Rev. C **90**, 024613 (2014).
- [65] S. Ayik, B. Yilmaz, and O. Yilmaz, Multinucleon exchange in quasifission reactions, Phys. Rev. C **92**, 064615 (2015).
- [66] S. Ayik, O. Yilmaz, B. Yilmaz, A.S. Umar, A. Gokalp, G. Turan, and D. Lacroix, Quantal description of nucleon exchange in a stochastic mean-field approach, Phys. Rev. C **91**, 054601 (2015).
- [67] S. Ayik, O. Yilmaz, B. Yilmaz, and A.S. Umar, Quantal nucleon diffusion: Central collisions of symmetric nuclei, Phys. Rev. C **94**, 044624 (2016).
- [68] S. Ayik, B. Yilmaz, O. Yilmaz, A.S. Umar, and G. Turan, Multinucleon transfer in central collisions of  $^{238}\text{U}+^{238}\text{U}$ , Phys. Rev. C **96**, 024611 (2017).
- [69] S. Ayik, B. Yilmaz, O. Yilmaz, and A.S. Umar, Quantal diffusion description of multinucleon transfers in heavy-ion collisions, Phys. Rev. C **97**, 054618 (2018).
- [70] B. Yilmaz, S. Ayik, O. Yilmaz, and A.S. Umar, Multinucleon transfer in  $^{58}\text{Ni}+^{60}\text{Ni}$  and  $^{60}\text{Ni}+^{60}\text{Ni}$  in a stochastic mean-field approach, Phys. Rev. C **98**, 034604 (2018).
- [71] S. Ayik, B. Yilmaz, O. Yilmaz, and A.S. Umar, Quantal diffusion approach for multinucleon transfers in Xe + Pb collisions, Phys. Rev. C **100**, 014609 (2019).
- [72] S. Ayik, O. Yilmaz, B. Yilmaz, and A.S. Umar, Heavy-isotope production in  $^{136}\text{Xe}+^{208}\text{Pb}$  collisions at  $E_{c.m.} = 514$  MeV, Phys. Rev. C **100**, 044614 (2019).
- [73] O. Yilmaz, G. Turan, and B. Yilmaz, Quasi-fission and fusion-fission reactions in  $^{48}\text{Ca}+^{208}\text{Pb}$  collisions at  $E_{c.m.} = 190$  MeV, Eur. Phys. J. A **56**, 37 (2020).
- [74] S. Ayik, N. Er, O. Yilmaz, and A. Gokalp, Quantal effects on spinodal instabilities in charge asymmetric nuclear matter, Nucl. Phys. **A812**, 44 (2008).
- [75] S. Ayik, O. Yilmaz, N. Er, A. Gokalp, and P. Ring, Spinodal instabilities in nuclear matter in a stochastic relativistic mean-field approach, Phys. Rev. C **80**, 034613 (2009).
- [76] S. Ayik, O. Yilmaz, F. Acar, B. Danisman, N. Er, and A. Gokalp, Investigations of instabilities in nuclear matter in stochastic relativistic models, Nucl. Phys. **A859**, 73 (2011).
- [77] O. Yilmaz, S. Ayik, and A. Gokalp, Quantal description of instabilities in nuclear matter in a stochastic relativistic model,

- Eur. Phys. J. A **47**, 123 (2011).
- [78] O. Yilmaz, S. Ayik, F. Acar, S. Saatici, and A. Gokalp, Investigations of spinodal dynamics in asymmetric nuclear matter within a stochastic relativistic model, *Eur. Phys. J. A* **49**, 33 (2013).
- [79] O. Yilmaz, S. Ayik, F. Acar, and A. Gokalp, Growth of spinodal instabilities in nuclear matter, *Phys. Rev. C* **91**, 014605 (2015).
- [80] F. Acar, S. Ayik, O. Yilmaz, and A. Gokalp, Growth of spinodal instabilities in nuclear matter. II. Asymmetric matter, *Phys. Rev. C* **92**, 034605 (2015).
- [81] D. Lacroix, S. Ayik, and B. Yilmaz, Symmetry breaking and fluctuations within stochastic mean-field dynamics: Importance of initial quantum fluctuations, *Phys. Rev. C* **85**, 041602(R) (2012).
- [82] D. Lacroix, S. Hermanns, C.M. Hinz, and M. Bonitz, Ultrafast dynamics of finite Hubbard clusters: A stochastic mean-field approach, *Phys. Rev. B* **90**, 125112 (2014).
- [83] Y. Tanimura, D. Lacroix, and S. Ayik, Microscopic Phase-Space Exploration Modeling of  $^{258}\text{Fm}$  Spontaneous Fission, *Phys. Rev. Lett.* **118**, 152501 (2017); *ibid.* **121**, 059902(E) (2018).
- [84] A. Bulgac, S. Jin, and I. Stetcu, Unitary evolution with fluctuations and dissipation, *Phys. Rev. C* **100**, 014615 (2019).
- [85] W. Królas, R. Broda, B. Fornal, T. Pawlat, H. Grawe, K.H. Maier, M. Schramm, and R. Schubart, Gamma coincidence study of  $^{208}\text{Pb} + 350\text{ MeV } ^{64}\text{Ni}$  collisions, *Nucl. Phys. A* **724**, 289 (2003).
- [86] W. Królas, R. Broda, B. Fornal, T. Pawlat, J. Wrzesiński, D. Bazzacco, G. de Angelis, S. Lunardi, R. Menegazzo, D.R. Napoli, C. Rossi Alvarez, Dynamical deformation of nuclei in deep-inelastic collisions: A gamma coincidence study of  $^{130}\text{Te} + 275\text{ MeV } ^{64}\text{Ni}$  and  $^{208}\text{Pb} + 345\text{ MeV } ^{58}\text{Ni}$  heavy ion reactions, *Nucl. Phys. A* **832**, 170 (2010).
- [87] J.W. Negele, The mean-field theory of nuclear structure and dynamics, *Rev. Mod. Phys.* **54**, 913 (1982).
- [88] T. Nakatsukasa, K. Matsuyanagi, M. Matsuo, and K. Yabana, Time-dependent density-functional description of nuclear dynamics, *Rev. Mod. Phys.* **88**, 045004 (2016).
- [89] T. Nakatsukasa and K. Yabana, Liner response theory in the continuum for deformed nuclei: Green's function vs time-dependent Hartree-Fock with the absorbing boundary condition, *Phys. Rev. C* **71**, 024301 (2005).
- [90] A.S. Umar and V.E. Oberacker, Time-dependent response calculations of nuclear resonances, *Phys. Rev. C* **71**, 034314 (2005).
- [91] J.A. Maruhn, P.G. Reinhard, P.D. Stevenson, J. Rikovska Stone, and M.R. Strayer, Dipole giant resonances in deformed heavy nuclei, *Phys. Rev. C* **71**, 064328 (2005).
- [92] S. Ebata, T. Nakatsukasa, T. Inakura, K. Yoshida, Y. Hashimoto, and K. Yabana, Canonical-basis time-dependent Hartree-Fock-Bogoliubov theory and linear-response calculations, *Phys. Rev. C* **82**, 034306 (2010).
- [93] S. Fracasso, E.B. Suckling, and P.D. Stevenson, Unrestricted Skyrme-tensor time-dependent Hartree-Fock model and its application to the nuclear response from spherical to triaxial nuclei, *Phys. Rev. C* **86**, 044303 (2012).
- [94] C.I. Pardi and P.D. Stevenson, Continuum time-dependent Hartree-Fock method for giant resonances in spherical nuclei, *Phys. Rev. C* **87**, 014330 (2013).
- [95] G. Scamps and D. Lacroix, Systematics of isovector and isoscalar giant quadrupole resonances in normal and superfluid spherical nuclei, *Phys. Rev. C* **88**, 044310 (2013).
- [96] G. Scamps and D. Lacroix, Systematic study of isovector and isoscalar giant quadrupole resonances in normal and superfluid deformed nuclei, *Phys. Rev. C* **89**, 034314 (2014).
- [97] S. Ebata, T. Nakatsukasa, and T. Inakura, Systematic investigation of low-lying dipole modes using the canonical-basis time-dependent Hartree-Fock-Bogoliubov theory, *Phys. Rev. C* **90**, 024303 (2014); *ibid.* **92**, 049902(E) (2015).
- [98] A.S. Umar, V.E. Oberacker, and J.A. Maruhn, Neutron transfer dynamics and doorway to fusion in time-dependent Hartree-Fock theory, *Eur. Phys. J. A* **37**, 245 (2008).
- [99] Y. Iwata, T. Otsuka, J.A. Maruhn, and N. Itagaki, Suppression of Charge Equilibration Leading to the Synthesis of Exotic Nuclei, *Phys. Rev. Lett.* **104**, 252501 (2010).
- [100] M. Evers, M. Dasgupta, D.J. Hinde, D.H. Luong, R. Rafiei, R. du Rietz, and C. Simenel, Cluster transfer in the reaction  $^{16}\text{O} + ^{208}\text{Pb}$  at energies well below the fusion barrier: A possible doorway to energy dissipation, *Phys. Rev. C* **84**, 054614 (2011).
- [101] K. Sekizawa and S. Heinz, Quasifission Dynamics and Stability of Superheavy Systems, *Acta Phys. Pol. B Proc. Suppl.* **10**, 225 (2017).
- [102] D.J. Kedziora and C. Simenel, New inverse quasifission mechanism to produce neutron-rich transfermium nuclei, *Phys. Rev. C* **81**, 044613 (2010).
- [103] C. Simenel, D.J. Hinde, R. du Rietz, M. Dasgupta, M. Evers, C.J. Lin, D.H. Luong, and A. Wakhle, Influence of entrance-channel magicity and isospin on quasi-fission, *Phys. Lett. B* **710**, 607 (2012).
- [104] A. Wakhle, C. Simenel, D.J. Hinde, M. Dasgupta, M. Evers, D.H. Luong, R. du Rietz, and E. Williams, Interplay between Quantum Shells and Orientation in Quasifission, *Phys. Rev. Lett.* **113**, 182502 (2014).
- [105] V.E. Oberacker, A.S. Umar, and C. Simenel, Dissipative dynamics in quasifission, *Phys. Rev. C* **90**, 054605 (2014).
- [106] A.S. Umar and V.E. Oberacker, Time-dependent HF approach to SHE dynamics, *Nucl. Phys. A* **944**, 238 (2015).
- [107] K. Washiyama, Microscopic analysis of fusion hindrance in heavy nuclear systems, *Phys. Rev. C* **91**, 064607 (2015).
- [108] A.S. Umar, V.E. Oberacker, and C. Simenel, Shape evolution and collective dynamics of quasifission in the time-dependent Hartree-Fock approach, *Phys. Rev. C* **92**, 024621 (2015).
- [109] A.S. Umar, V.E. Oberacker, and C. Simenel, Fusion and quasifission dynamics in the reactions  $^{48}\text{Ca} + ^{249}\text{Bk}$  and  $^{50}\text{Ti} + ^{249}\text{Bk}$  using a time-dependent Hartree-Fock approach, *Phys. Rev. C* **94**, 024605 (2016).
- [110] C. Yu and Lu Guo, Angular momentum dependence of quasifission dynamics in the reaction  $^{48}\text{Ca} + ^{244}\text{Pu}$ , *Sci. China Phys. Mech. Astron.* **60**, 092011 (2017).
- [111] H. Zheng, S. Burrello, M. Colonna, D. Lacroix, and G. Scamps, Connecting the nuclear equation of state to the interplay between fusion and quasifission processes in low-energy nuclear reactions, *Phys. Rev. C* **98**, 024622 (2018).
- [112] R. Keser, A.S. Umar, and V.E. Oberacker, Microscopic study of Ca + Ca fusion, *Phys. Rev. C* **85**, 044606 (2012).
- [113] C. Simenel, R. Keser, A.S. Umar, and V.E. Oberacker, Microscopic study of  $^{16}\text{O} + ^{16}\text{O}$  fusion, *Phys. Rev. C* **88**, 024617 (2013).
- [114] P.-G. Reinhard, A.S. Umar, P.D. Stevenson, J. Piekarewicz, V.E. Oberacker, and J.A. Maruhn, Sensitivity of the fusion cross section to the density dependence of the symmetry energy, *Phys. Rev. C* **93**, 044618 (2016).
- [115] K. Godbey, A. S. Umar, and C. Simenel, Dependence of fusion on isospin dynamics, *Phys. Rev. C* **95**, 011601(R) (2017).



- [116] Lu Guo, K. Godbey, and A.S. Umar, Influence of the tensor force on the microscopic heavy-ion interaction potential, *Phys. Rev. C* **98**, 064607 (2018).
- [117] C. Simenel, Ph. Chomaz, and G. de France, Fusion process studied with a preequilibrium giant dipole resonance in time-dependent Hartree-Fock theory, *Phys. Rev. C* **76**, 024609 (2007).
- [118] D. Bourgin, C. Simenel, S. Courtin, and F. Haas, Microscopic study of  $^{40}\text{Ca}+^{58,64}\text{Ni}$  fusion reactions, *Phys. Rev. C* **93**, 034604 (2016).
- [119] K. Vo-Phuoc, C. Simenel, and E.C. Simpson, Dynamical effects in fusion with exotic nuclei, *Phys. Rev. C* **94**, 024612 (2016).
- [120] C. Simenel and A.S. Umar, Formation and dynamics of fission fragments, *Phys. Rev. C* **89**, 031601(R) (2014).
- [121] G. Scamps, C. Simenel, and D. Lacroix, Superfluid dynamics of  $^{258}\text{Fm}$  fission, *Phys. Rev. C* **92**, 011602(R) (2015).
- [122] Y. Tanimura, D. Lacroix, and G. Scamps, Collective aspects deduced from time-dependent microscopic mean-field with pairing: Application to the fission process, *Phys. Rev. C* **92**, 034601 (2015).
- [123] P. Goddard, P. Stevenson, and A. Rios, Fission dynamics within time-dependent Hartree-Fock: Deformation-induced fission, *Phys. Rev. C* **92**, 054610 (2015).
- [124] P. Goddard, P. Stevenson, and A. Rios, Fission dynamics within time-dependent Hartree-Fock. II. Boost-induced fission, *Phys. Rev. C* **93**, 014620 (2016).
- [125] G. Scamps and C. Simenel, Impact of pear-shaped fission fragments on mass-asymmetric fission in actinides, *Nature (London)* **564**, 382 (2018).
- [126] T. Nakatsukasa, Density functional approaches to collective phenomena in nuclei: Time-dependent density functional theory for perturbative and non-perturbative nuclear dynamics, *Prog. Theor. Exp. Phys.* **2012**, 01A207 (2012).
- [127] C. Simenel and A.S. Umar, Heavy-ion collisions and fission dynamics with the time-dependent Hartree-Fock theory and its extensions, *Prog. Part. Nucl. Phys.* **103**, 19 (2018).
- [128] P.D. Stevenson and M.C. Barton, Low-energy heavy-ion reactions and the Skyrme effective interaction, *Prog. Part. Nucl. Phys.* **104**, 142 (2019).
- [129] P. Ring and P. Schuck, *The Nuclear Many-Body Problem* (Springer Verlag, New York, 1980).
- [130] J.L. Egido, State-of-the-art of beyond mean field theories with nuclear density functionals, *Phys. Scr.* **91**, 073003 (2016).
- [131] I. Ulgen, B. Yilmaz, and D. Lacroix, Impact of initial fluctuations on the dissipative dynamics of interacting Fermi systems: A model case study, *Phys. Rev. C* **100**, 054603 (2019).
- [132] B. Yilmaz, D. Lacroix, and R. Currey, Importance of realistic phase-space representations of initial quantum fluctuations using the stochastic mean-field approach for fermions, *Phys. Rev. C* **90**, 054617 (2014).
- [133] J. Randrup, Theory of transfer-induced transport in nuclear collisions, *Nucl. Phys.* **A327**, 490 (1979).
- [134] W.U. Schröder, J.R. Huizenga, and J. Randrup, Correlated mass and charge transport induced by statistical nucleon exchange in damped nuclear reactions, *Phys. Lett.* **B98**, 355 (1981).
- [135] A.C. Merchant and W. Nörenberg, Neutron and proton diffusion in heavy-ion collisions, *Phys. Lett.* **B104**, 15 (1981).
- [136] H. Feldmeier, Transport phenomena in dissipative heavy-ion collisions: the one-body dissipation approach, *Rep. Prog. Phys.* **50**, 915 (1987).
- [137] C.W. Gardiner, *Quantum Noise* (Springer-Verlag, Berlin, 1991).
- [138] U. Weiss, *Quantum Dissipative Systems*, 2nd ed. (World Scientific, Singapore, 1999).
- [139] H. Risken and T. Frank, *The Fokker-Plank Equation* (Springer-Verlag, Berlin, 1996).
- [140] D. Hilscher, J.R. Birkelund, A.D. Hoover, W.U. Schröder, W.W. Wilcke, J.R. Huizenga, A.C. Mignerey, K.L. Wolf, H.F. Breuer, and V.E. Viola, Jr., Neutron emission in the reaction  $^{165}\text{Ho}+^{56}\text{Fe}$  at  $E_{\text{lab}} = 8.5\text{ MeV/u}$ , *Phys. Rev. C* **20**, 576 (1979).
- [141] R. Vandenbosch, A. Lazzarini, D. Leach, D.-K. Lock, A. Ray, and A. Seamster, Nonequilibrium Excitation-Energy Division in Deeply Inelastic Collisions, *Phys. Rev. Lett.* **52**, 1964 (1984).
- [142] R.J. Charity, in *Joint ICTP-IAEA Advanced Workshop on Model Codes for Spallation Reactions, Trieste, Italy, 2008* (IAEA, Vienna, 2008), pp. 139–148; The GEMINI++ code can be downloaded from: <https://bitbucket.org/arekfu/gemini>.
- [143] R.J. Charity, Systematic description of evaporation spectra for light and heavy compound nuclei, *Phys. Rev. C* **82**, 014610 (2010).
- [144] D. Mancusi, R.J. Charity, and J. Cugnon, Unified description of fission in fusion and spallation reactions, *Phys. Rev. C* **82**, 044610 (2010).
- [145] K.-H. Kim, T. Otsuka, and P. Bonche, Three-dimensional TDHF calculations for reactions of unstable nuclei, *J. Phys. G: Nucl. Part. Phys.* **23**, 1267 (1997).
- [146] C. Simenel, A.S. Umar, K. Godbey, M. Dasgupta, and D.J. Hinde, How the Pauli exclusion principle affects fusion of atomic nuclei, *Phys. Rev. C* **95**, 031601(R) (2017).
- [147] A complete list of full movies can be found in: <https://www.youtube.com/playlist?list=PLKTMVRARzsqUKpMiOXAzliVSGzjD0ZG2>.
- [148] L. Corradi, J.H. He, D. Ackermann, A.M. Stefanini, A. Pisent, S. Beghini, G. Montagnoli, F. Scarlassara, G.F. Segato, G. Pollarolo, C.H. Dasso, and A. Winther, Multinucleon transfer reactions in  $^{40}\text{Ca}+^{124}\text{Sn}$ , *Phys. Rev. C* **54**, 201 (1996).
- [149] L. Corradi, A.M. Stefanini, C.J. Lin, S. Beghini, G. Montagnoli, F. Scarlassara, G. Pollarolo, and A. Winther, Multinucleon transfer processes in  $^{64}\text{Ni}+^{238}\text{U}$ , *Phys. Rev. C* **59**, 261 (1999).
- [150] S. Szilner, L. Corradi, G. Pollarolo, S. Beghini, B.R. Behera, E. Fioretto, A. Gadea, F. Haas, A. Latina, G. Montagnoli, F. Scarlassara, A.M. Stefanini, M. Trotta, A.M. Vinodkumar, and Y. Wu, Multinucleon transfer processes in  $^{40}\text{Ca}+^{208}\text{Pb}$ , *Phys. Rev. C* **71**, 044610 (2005).
- [151] L. Corradi, A.M. Vinodkumar, A.M. Stefanini, E. Fioretto, G. Prete, S. Beghini, G. Montagnoli, F. Scarlassara, G. Pollarolo, F. Cerutti, and A. Winther, Light and heavy transfer products in  $^{58}\text{Ni}+^{208}\text{Pb}$  at the Coulomb barrier, *Phys. Rev. C* **66**, 024606 (2002).
- [152] T. Mijatović, S. Szilner, L. Corradi, D. Montanari, G. Pollarolo, E. Fioretto, A. Gadea, A. Goasduff, D. Jelavić Malenica, N. Märginean, M. Milin, G. Montagnoli, F. Scarlassara, N. Soić, A.M. Stefanini, C.A. Ur, and J.J. Valiente-Dobón, Multinucleon transfer reactions in the  $^{40}\text{Ar}+^{208}\text{Pb}$  system, *Phys. Rev. C* **94**, 064616 (2016).
- [153] Y.X. Watanabe, Y.H. Kim, S.C. Jeong, Y. Hirayama, N. Imai, H. Ishiyama, H.S. Jung, H. Miyatake, S. Choi, J.S. Song, E. Clement, G. de France, A. Navin, M. Rejmund, C. Schmitt, G. Pollarolo, L. Corradi, E. Fioretto, D. Montanari, M. Niikura, D. Suzuki, H. Nishibata, and J. Takatsu, Pathway for the Production of Neutron-Rich Isotopes around the  $N=126$  Shell Closure, *Phys. Rev. Lett.* **115**, 172503 (2015).

- [154] Y. Hashimoto and G. Scamps, Gauge angle dependence in time-dependent Hartree-Fock-Bogoliubov calculations of  $^{20}\text{O}+^{20}\text{O}$  head-on collisions with the Gogny interaction, *Phys. Rev. C* **94**, 014610 (2016).
- [155] P. Magierski, K. Sekizawa, and G. Wlazłowski, Novel Role of Superfluidity in Low-Energy Nuclear Reactions, *Phys. Rev. Lett.* **119**, 042501 (2017).
- [156] K. Sekizawa, P. Magierski, and G. Wlazłowski, Solitonic Excitations in Collisions of Superfluid Nuclei, *PoS (INPC2016)* 214 (2017).
- [157] K. Sekizawa, G. Wlazłowski, and P. Magierski, Solitonic excitations in collisions of superfluid nuclei: a qualitatively new phenomenon distinct from the Josephson effect, *EPJ Web of Conf.* **163**, 00051 (2017).
- [158] M.C. Barton, S. Jin, P. Magierski, K. Sekizawa, G. Wlazłowski, and A. Bulgac, Pairing dynamics in low energy nuclear collisions, *Acta Phys. Pol. B* **51**, 605 (2020).
- [159] D. Lacroix, D. Gambacurta, and S. Ayik, Quantal corrections to mean-field dynamics including pairing, *Phys. Rev. C* **87**, 061302(R) (2013).
- [160] J.C. Pei, G.I. Fann, R.J. Harrison, W. Nazarewicz, Y. Shi, and S. Thornton, Adaptive multi-resolution 3D Hartree-Fock-Bogoliubov solver for nuclear structure, *Phys. Rev. C* **90**, 024317 (2014).
- [161] S. Jin, A. Bulgac, K. Roche, and G. Wlazłowski, Coordinate-space solver for superfluid many-fermion systems with the shifted conjugate-orthogonal conjugate-gradient method, *Phys. Rev. C* **95**, 044302 (2017).
- [162] Y. Shi, Precision of finite-difference representation in 3D coordinate-space Hartree-Fock-Bogoliubov calculations, *Phys. Rev. C* **98**, 014329 (2018).
- [163] Yu Kashiwaba and T. Nakatsukasa, Coordinate-space solver for finite-temperature Hartree-Fock-Bogoliubov calculations using the shifted Krylov method, *Phys. Rev. C* **101**, 045804 (2020).
- [164] G. Scamps, D. Lacroix, G.F. Bertsch, and K. Washiyama, Pairing dynamics in particle transport, *Phys. Rev. C* **85**, 034328 (2012).
- [165] G. Scamps and D. Lacroix, Effect of pairing on one- and two-nucleon transfer below the Coulomb barrier: A time-dependent microscopic description, *Phys. Rev. C* **87**, 014605 (2013).
- [166] S. Ebata and T. Nakatsukasa, Repulsive Aspects of Pairing Correlation in Nuclear Fusion Reaction, *JPS Conf. Proc.* **6**, 020056 (2015).
- [167] G. Scamps and Y. Hashimoto, Transfer probabilities for the reactions  $^{14,20}\text{O}+^{20}\text{O}$  in terms of multiple time-dependent Hartree-Fock-Bogoliubov trajectories, *Phys. Rev. C* **96**, 031602(R) (2017).
- [168] T. Czuba, D. Lacroix, D. Regnier, I. Ulgen, and B. Yilmaz, Combining phase-space and time-dependent reduced density matrix approach to describe the dynamics of interacting fermions, *Eur. Phys. J. A* **56**, 111 (2020).
- [169] A.C. Merchant and W. Nörenberg, Microscopic Transport Theory of Heavy-Ion Collisions, *Z. Phys. A* **308**, 315 (1982).